Supporting Information

Light-Activated Intercluster Conversion of an Atomically Precise Silver Nanocluster

Arijit Jana[ξ], Madhuri Jash[ξ], Ajay Kumar Poonia[€], Ganesan Paramasivam[ξ], Md Rabiul Islam[ξ], Papri Chakraborty[ξ], Sudhadevi Antharjanam[δ], Jan Machacek [ψ], Sundargopal Ghosh[ξ], Kumaran Nair Valsala Devi Adarsh* [€], Tomas Base* [ψ], and Thalappil Pradeep* [ξ]

[ξ] DST Unit of Nanoscience (DST UNS), and Thematic Unit of Excellence (TUE), Department of Chemistry, Indian Institute of Technology, Madras, Chennai – 600036, India

[ψ] Department of Synthesis, Institute of Inorganic Chemistry, The Czech Academy of Science, 1001 Husinec-Rez, 25068, Czech Republic

[€]Department of Physics, Indian Institute of Science Education, and Research Bhopal, Bhopal-462066, India

[δ]Sophisticated Analytical Instruments Facility (SAIF), Indian Institute of Technology, Madras, Chennai – 600036, India

*Email: pradeep@iitm.ac.in, tbase@iic.acs.cz, adarsh@iiserb.ac.in

Table of contents:

Experimental section

Chemicals

Ortho-carborane-1, 2-dithiol (CBDT) was synthesized by following the previous literature.[1,2] As synthesized CBDT was further purified using crystallization from hot dichloromethane/hexane (1:1) solution. Silver nitrate ($AgNO_3$) was purchased from Rankem chemicals. Sodium borohydride ($NaBH_4$, 98%), and triphenylphosphine (TPP) were purchased from Aldrich chemicals. Solvent grade dichloromethane (DCM), chloroform ($CHCl_3$), n-hexane, N-N dimethyl-formamide (DMF), and methanol (99.5%) were purchased from Rankem chemicals and Finar, India. Milli-Q water was used for $[Ag_{18}H_{16}(TPP)_{10}]^{2+}$ NC synthesis purpose. Deuterated solvent, $CDCl_3$ (99.8 atom % D) was purchased from Sigma Aldrich. All the chemicals are commercially available and used as such without further purification.

Synthesis of $[Ag_{18}H_{16}(TPP)_{10}]^{2+}$ NC

Ag_{18} NC was synthesized by following the previous literatures.[3,4] Briefly, in room temperature, 20 mg of $AgNO_3$ was dissolve in 5 mL of methanol. After that, 70 mg of TPP was dissolved in 9 mL of $CHCl_3$ and was added to the reaction mixture under stirring condition. After 20 min of reaction, 6.5 mg $NaBH_4$, dissolved in 0.75 mL of milli-Q water was added to it. After addition of $NaBH_4$, reaction mixture becomes yellow solution, which gradually converted to dark brownish solution, and finally after 3.5 hours it becomes dark green color which indicates the formation of Ag_{18} NC. After completion of the reaction, mixed solvents were removed under reduced pressure. Dark greenish NC was dissolved in cold water to remove excess salts. Finally, the purified Ag_{18} NC was extracted using methanol. Formation of the NC was confirmed from their UV-vis absorption spectra and mass spectrometric results are shown in Figure S1. The yield of the reaction is 20% in terms of silver. The same NC was used for the synthesis of Ag_{42} NC.

Synthesis of $[Ag_{42}(CBDT)_{15}(TPP)_4]^{2-}$ NC

Ag_{42} was synthesized by following ligand exchange induced structural transformation (LEIST) reaction between Ag_{18}, and *ortho*-carborane-1, 2-dithiol (CBDT) ligand. During the synthesis, at first 5.5 mg of CBDT was dissolved in 1 mL of methanol. Then it was quickly added to the methanol solution of Ag_{18} (3 mg/mL) under 800 rpm stirring condition. Just after the addition of the ligand, a greenish-white precipitate was formed. After 4 hours of continuous reaction, the white precipitate was slowly converts to the brownish precipitate, which indicates the formation of Ag_{42}. After completion of the reaction, brownish precipitate was cleaned three times each using methanol and ethanol to remove the excess phosphines. Then the precipitate was vacuum dried, and Ag_{42} was extracted by dissolving the precipitate in dichloromethane or chloroform or dimethylformamide for further characterizations. Yield of the product is 60 to 65 % in terms of silver.

Thermal treatment of Ag_{42} NC

Thermal stability of the Ag_{42} cluster in its solid state was measured upon dropcasting 10 mg of purified cluster. After 24 h of heating, we have measured its UV-vis absorption spectrum upon dissolving the cluster in DCM. Figure S16 shows absorption spectrum of the cluster after each

heating. To understand the thermal stability of the Ag_{42} in solution at ambient condition, 10 mg of NC soluble in 5 mL of DMF solvent was used for heat treatment. Each step of the heating experiment was performed for up to 24 hours at 600 rpm stirring condition. Photographs of the solution and the respective UV-vis absorption spectra of each step are shown in Figure S26.

Instrumentation

UV-vis absorption spectroscopy

UV-vis absorption spectra were measured using Perkin Elmer Lambda 365 UV-vis spectrometer in the wavelength region of 200 to 1100 nm.

ESI-MS

Mass spectrum of *ortho*-carborane-1, 2-dithiol was measured using Thermo Scientific LTQ XL Linear ion Trap Mass spectrometer. Mass spectra of all the nanoclusters were measured using Waters Synapt G2Si HDMS instrument. Ag_{18} NC mass spectrum was collected in positive ion mode, and Ag_{42}, Int. I, Int. II, Ag_{14} NCs mass spectra were collected in negative ion mode. All the MS/MS or fragmentation experiments were performed by varying the collision energy of the selected ions inside the trap cell using the G2Si instrument. An optimized condition of flow rate: 20 µL/min, capillary voltage: 2.5 - 3 kV, cone voltage: 0 V, source temperature: 70-100 ^{o}C were used to record these ESI-MS spectra measurements.

Photoluminescence spectroscopy

Photoluminescence spectra were measured using Jobin Yvon Nanolog fluorescence spectrometer.

X-ray photoelectron spectroscopy

X-ray photoelectron spectroscopy was recorded using ESCA probe TPD equipped with polychromatic Mg Kα X ray source ($h\gamma$ = 1253.6 eV). Purified cluster solution made in DCM was drop casted on a sample grid for the measurements.

FT-IR spectroscopy

FT-IR spectra were recorded using JASCO FT-IR 4100 spectrometer after preparing sample pallets using potassium bromide.

NMR spectroscopy

Multinuclear NMR spectra of the samples were measured using Bruker 500 MHz FT-NMR spectrometer. Around 20-25 mg of NC soluble in 0.75 mL of $CDCl_3$ solvent was used for measurements. Spectra were processed using MestRe-Nova NMR software.

Powder XRD

Powder XRD of the Ag_{42} NC was measured using a D8 Advance Bruker instrument, using Cu Kα as the X-ray source ($h\gamma$ = 8047.8 eV).

Thermogravimetric analysis (TGA) and derivative thermogravimetric (DTG), and differential scanning calorimetry (DSC) analysis

Thermogravimetric (TG) measurements of about 3.821 mg of NC sample in an alumina crucible were performed using a NETZSCH STA 449 F3 Jupiter instruments equipped with Proteus-6.1.0 software. The measurements were performed under nitrogen atmosphere at a flow rate of 20 mL/min in the temperature range of 30 to 600 °C with a heating rate of 10 °C/min. The DSC study was performed using the same instrument.

TCSPC measurements

The time-resolved PL lifetime measurements were performed using HORIBA DeltaFlex TCSPC lifetime spectrofluorometer. The spectrometer was coupled with ps pulses diode lasers (pulse width of 85 ps) with excitation wavelength centred at 530 nm and 400 nm for Ag_{42} and Ag_{14} NCs, respectively. For visible region HORIBA PPD-850 detector, and for NIR region HAMAMATSU PMT detector is employed. The instrument response function is shown in Figure S43.

Femtosecond pump-probe measurements

In fs-TA measurement, ultrafast short laser of pulse width 120 fs centred at 800 nm are generated by spectra physics Maitai oscillator with the energy of few hundreds of nJ. The output beam send to Ti: sapphire optical amplifier system to produce high energy pulses (4 mJ/pulses, pulse width 120 fs, repetition rate 1 kHz). The output beam is further split into two parts, the first high energy beam is used to produce the second harmonic using β-barium borate crystal. The obtained 400 nm pulses are employed to excite the sample with the intensity of 250 μJ/cm^2. Other weak part of beam is used to generate the white light continuum probe pulses by CaF_2 crystal (450-800 nm). The computer-controlled motion controller is used to create the delay between pump-probe. The absorbance changes in the probe beam due to pump is calculated using the equation-

$$\Delta A = \log[I_{ex}(s)/I_0(s)] - [I_{ex}(r)/I_0(r)]$$

Where r and s correspond to the reference and sample, I_{ex} and I_o are transmitted intensities of probe pulse after excitation and in ground state, respectively. The intensity of transmitted pulse are measured with the help of MS 2004 (600 lines/mm diffraction grating blazed at 600 nm) spectrometer, and Si linear photodiode arrays. To compensate for the group velocity dispersion, the obtained TA spectra are chirp corrected. The ethanol is used to measure the magnitude of chirp.

Nanosecond flash photolysis

In ns pump-probe measurement, we excite the sample using the second harmonic of Nd-YAG laser with pulse width of 5 ns (spectra physics). To monitor the change in absorbance the white light (500-800) is produced using Xenon-Arc lamp (150 W) which is aligned in cross beam configuration to the pulp laser beam. Laser flash photolysis spectrometer (LKS80Applied Photo physics) with the combination of oscilloscope (Agilent Infinium DSO9064A) is used to measure the change in absorbance.

Optical microscopy

Optical microscopic images of the crystals in 10X magnification were collected using LEICA optical microscope equipped with LAS V4.8 software. Polarizer, and without polarizer mode was used to collect the images.

Scanning electron microscopy (SEM)

SEM imaging was performed using FEI quanta environmental scanning electron microscope (ESEM) at high vacuum mode, at operating voltage of 30 kV. Energy dispersive X-ray analysis (EDS) spectra and elemental mapping were recorded using the same instrument.

Transmission electron microscopy (TEM)

TEM imaging and size analysis of the nanoclusters were performed using a JEOL 3010, 300 kV instrument at an accelerating voltage of 200 kV. The accelerating voltage was kept low to reduce beam-induced damage. Samples were prepared by drop casting the solution of the clusters on carbon-coated copper grids and dried under ambient conditions. EDS spectra were collected using the same instrument.

Crystallographic details

Single-crystal X-ray diffraction (SC-XRD) data collection was performed at 293 K using Bruker D8 VENTURE SC-XRD equipped with Mo Kα radiation source of wavelength 0.71073 Å, and a PHOTON 100 CMOS detector. A suitable crystal for SC-XRD analysis was mounted on a Kapton loop with the help of Paratone oil. The program APEX3-SAINT (Bruker, 2016) was used for integrating the frames. A multi-scan absorption correction was done using the program SADABS (Bruker, 2016). The structure was solved by SHELXT-2014 (Sheldrick, 2014), and refined by full-matrix least squares techniques using SHELXL-2018, (Sheldrick, 2018) computer program. Hydrogens on all carbon, and boron atoms were fixed at calculated positions, and refined as riding model with C—H = 0.93 Å, B-H = 1.10 Å, and U_{iso}(H) = 1.2 Ueq(C) or 1.2 Ueq(B). The molecule is crystallized in triclinic crystal system with P-1 space group. The asymmetric unit contains half of Ag_{14} nanocluster (Ag_{14} NC) and half of Ag_2-S-(triphenylphosphie)$_2$ (shortly, Ag_2S@TPP) moieties. The solvent electron density could not be modelled satisfactorily due to difficulty in locating their position. The observed R_{int} was high due to very weak diffraction of crystal at higher Bragg's angles. Therefore a resolution cut at ~1.0 Å was made during data reduction process to get a reasonable integration parameters in values/error models. Reflections above $\theta = 18^0$ were omitted during refinement to improve R_{int} to a reasonable value. Due to very high thermal and vibrational/rotational disorder of triphenylphosphine as well as carborane moieties, several restraints (DFIX, SIMU, ISOR, DELU *etc.*) were applied to their bond distances, and thermal parameters (U_{ij}) values during refinement to maintain sensible molecular geometry as well as reasonable anisotropic displacement parameter (ADPs) values. Moreover, FLAT restraint is needed to be applied for atoms in the phenyl ring to lie in a common plane. These factors prevent to get a quality data for these type of crystals for a good R values. It is to be noted here that, there are some literature reports for metal-organic frameworks (MOFs), which has this type of high R values.[5-7]

Several attempts were made to grow a better quality crystal for SC-XRD studies, but all failed miserably, and this is the best crystal we could obtain for single crystal studies. Also, attempt to collect data at low temperature was not successful as we could not observe any diffraction peaks at simple scan stage itself. This may be caused due to the collapse of crystal lattice at low temperatures. Although refinement parameters such as R1 = 0.1869, wR2 = 0.4247, Rint = 0.2609, *etc*., are high, the structure is presented here to show the formation of Ag_{14} nanocluster with the support of other experimental findings. A cif check report was made using the service of IUCR in which A and B level alerts were explained.

Computational details

The structural, electronic, and optical properties such as absorption spectra of the NCs are computationally studied using density functional theory (DFT) and time-dependent density functional theory (TDDFT) calculations. The atomic coordinates of its crystal structure were taken to initiate the geometric optimization using DFT and TDDFT as implemented in Grid-based Projector Augmented Wave method (GPAW) software package.[8,9] The exchange functional Pardew−Burke−Ernzerhof (PBE) functional was used in the real space grid to describe their optimized geometry and interactions in the cluster.[10] The grid spacing was kept at 0.2 Å. The atomic PAW setup describes the valence electrons for Ag ($4d^{10}$ $5s^1$ $5p^6$), S ($3s^2$ $3p^4$), P ($3s^2$ $3p^3$), C ($2s^2$ $2p^2$), B ($2s^2$ $2p^1$), and H ($1s^1$) with scalar-relativistic effects which were included for Ag. The convergence condition was to minimize the residual forces without any symmetry constraints by 0.05 eV/Å. The emission spectrum of the cluster was computed from the excited state optimized geometry of the cluster using delta SCF method.[11] All the structural visualizations of the NCs were done with visual molecular dynamics (VMD) software.

Ag_{14} NC structure optimization by DFT

The theoretically optimized structure of $[Ag_{14}(CBDT)_6(TPP)_6]$ NC in real space DFT was shown in Figure S41. The combination of TPP ligands with CBDT ligands restricts the TPP ligands to interact only at six edges of the cubic shell of the cluster. Here, the primary ligand is CBDT, and the secondary ligand is TPP. From the optimized structure, it is clear that the interaction of CBDT is responsible for the stability of the cluster. Further the primary ligand also controls the interaction of secondary ligand on the surface of the cluster. From Figure S42a, it is clear that with two sulfur atoms, the carborane ligand interacts with the core of the Ag_{14} cluster. However, the CBT ligands strongly interact with the Ag_6 core with the average bond distance of 2.56 Å rather than the shell. However, there is a significant distortion in the Ag(core)-S is found with the bond distances of 2.54 Å and 2.61 Å. Due to this interaction, the octahedral core is formed with two different Ag-Ag bond distances of 2.82 Å and 2.84 Å. The CBT ligands interaction with the cubic shell Ag atoms on the eight edges have two unique interactions, such as a strong interaction with the Ag-S bond distance of 2.63 Å on either Ag atom on the top and bottom of the cubic structure in which there is no secondary ligand interaction is observed. On the other hand, the Ag-S interaction with the Ag atom in which the P atom of the TPP ligands interacts is in general, a weak bonding interaction with the average bond distance of 2.67 Å starting from the bonding variation from 2.67 Å to 2.93 Å. It is noted from the geometry that the stabilization of the structure could be due to the asymmetric bonding interaction of S atoms of CBT ligands, and it may originate due to the two

main things. One is the charge difference between two S atoms of the same CBT ligand, and the second thing is due to the strong interaction of Ag-P interaction with the bond distance of 2.56 Å. Furthermore, the conjunction of both primary and secondary ligands on the surface of the cluster also does not allow accommodation of two more TPP ligands on two Ag atoms of the cubic shell, which are only interacting with the primary CBT ligands. It is noted from the geometry that the stabilization of the structure could be due to the asymmetric bonding interaction of S atoms of CBT ligands, and it may originate due to the two main things. One is the charge difference between two S atoms of the same CBT ligand, and the second thing is due to the strong interaction of Ag-P interaction with the bond distance of 2.56 Å. Furthermore, the conjunction of both primary and secondary ligands on the surface of the cluster also does not allow accommodation of two more TPP ligands on two Ag atoms of the cubic shell, which are only interacting with the primary CBDT ligands.

Theoretical calculation of IR Spectra

Quantum chemistry calculations were performed by the NWChem package.[12] The geometries were optimized and vibrational frequencies were calculated by means of the density functional theory with the hybrid exchange–correlation functional PBE0.[13-15] Jensen's double–zeta basis PC-1 was used.[16] The translations and rotations were projected out of the nuclear hessian using the standard Eckart algorithm.[17] The calculated frequencies and normal modes were examined with the help of the visualisation program Gabedit.[18] The vibrational spectra were simulated with Gabedit by the simple application of Lorentzian line shape of uniform arbitrary half width. The half width values of 15 cm^{-1} and 30 cm^{-1} respectively were used, as indicated in the Figure S15.

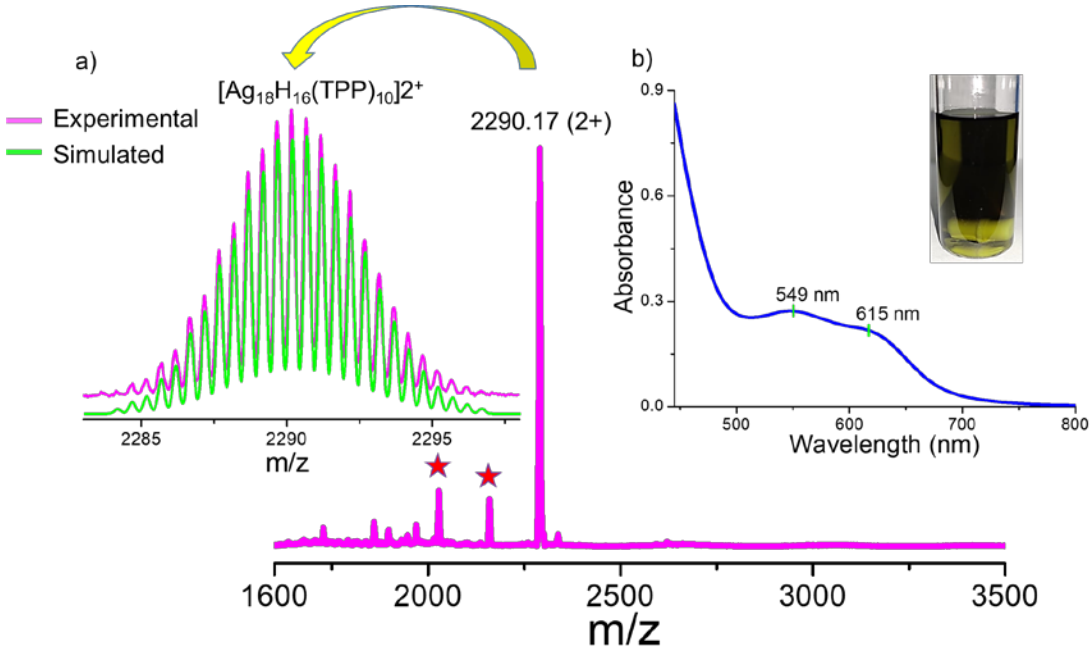

Figure S1. a) Positive ion-mode ESI-MS spectrum of the Ag_{18} NC. Each * indicates sequential TPP loss from the parent NC. Inset shows the exact matching of the isotopic distribution of the experimental and theoretical spectrum. b) UV-vis absorption spectrum of the Ag_{18} NC in methanol. Inset: photograph of the nanocluster in methanol.

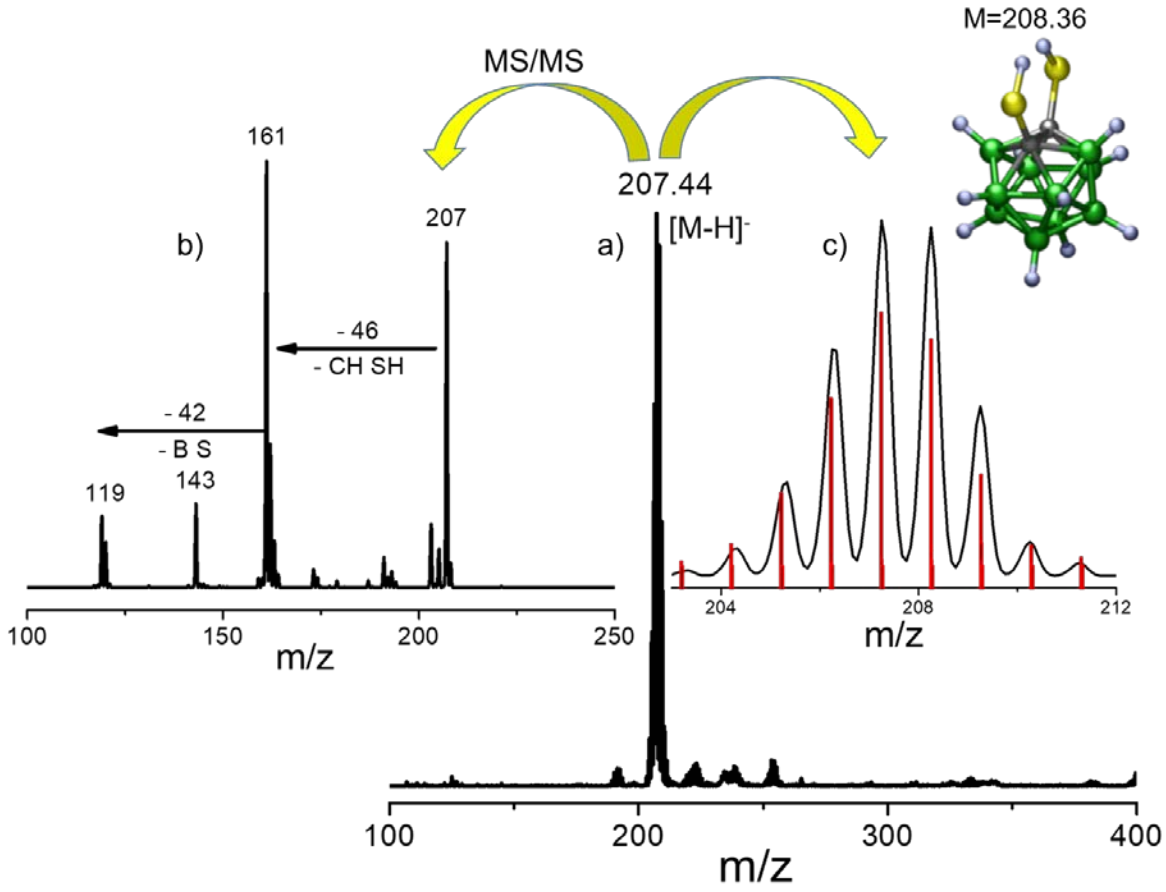

Figure S2. a) Negative ion-mode ESI-MS spectrum of the *ortho*-carborane-1, 2-dithiol ligand, b) MS/MS fragmentation pattern of the molecular ion peak at m/z 207.44, showing the loss of different fragments from the carborane moiety, c) exact matching of the isotopic distribution of the experimental spectrum with the theoretical spectrum.

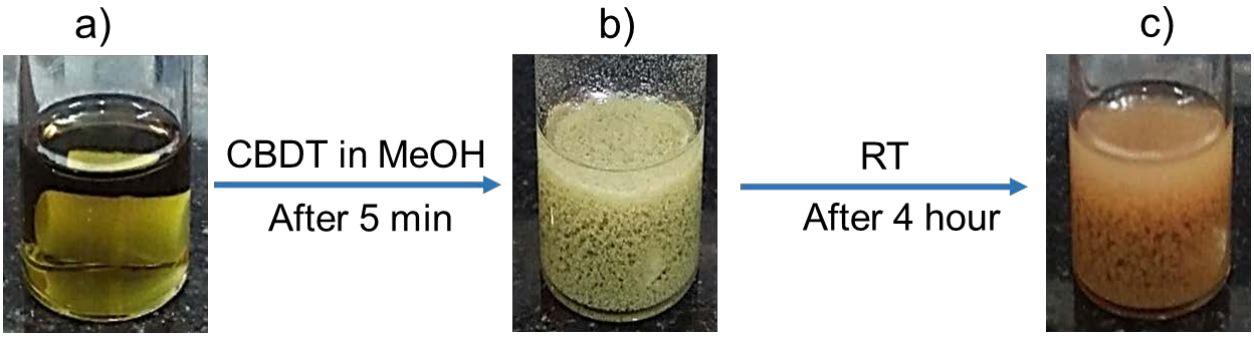

Figure S3. Digital photographs at the various stages of Ag_{42} synthesis; a) Ag_{18} in 5 ml methanol, b) after 5 min of the addition of the CBDT ligand, c) after 4 hours of the reaction at room temperature showed the color change during the reaction.

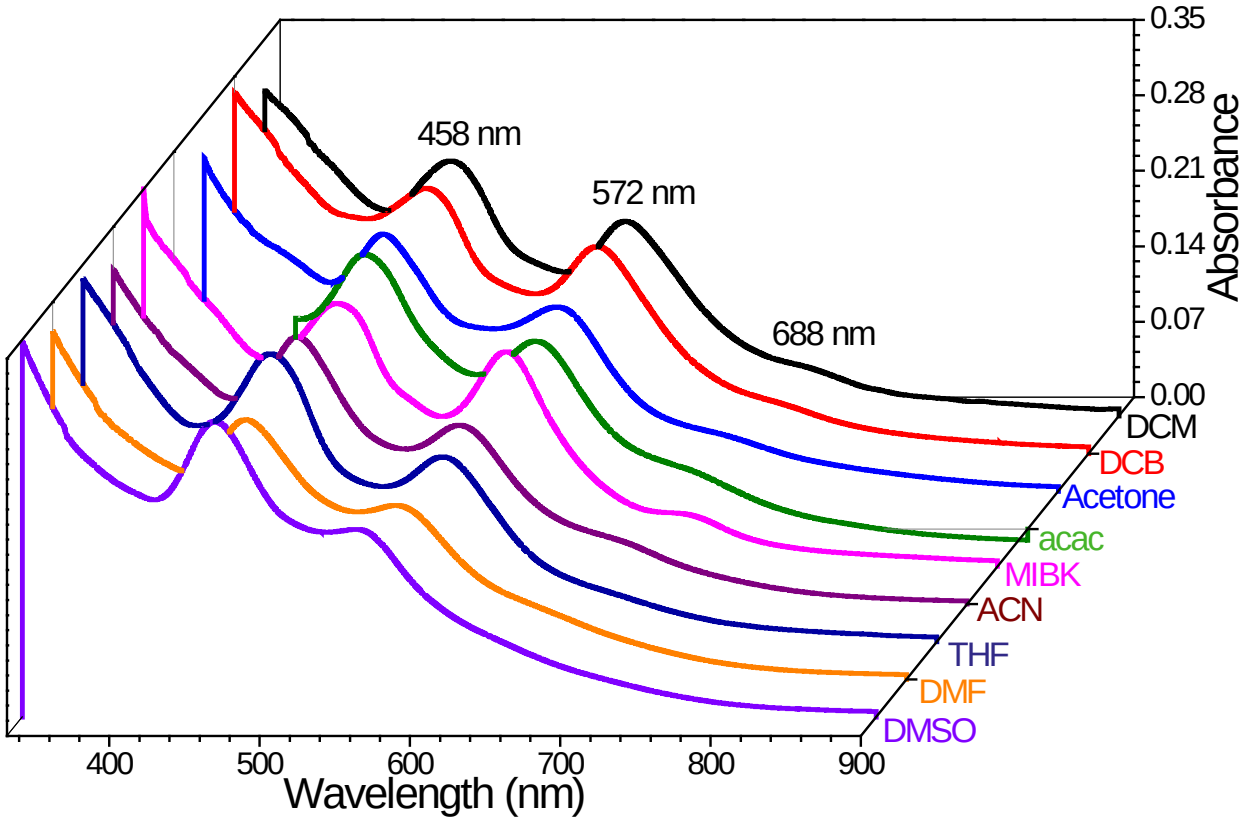

Figure S4. UV-vis absorption spectra of Ag_{42} nanocluster measured in different solvents. Broadening of absorption band at 572 nm was observed due to solvatochromic interaction with DMF, and DMSO. (Abbreviation: DCM = dichloromethane, DCB = 1, 2-dichlorobenzene, acac = acetyl acetone, MIBK = methyl isobutyl ketone, ACN = acetonitrile, THF = tetrahydrofuran, DMF = dimethyl formamide, DMSO = dimethyl sulfoxide).

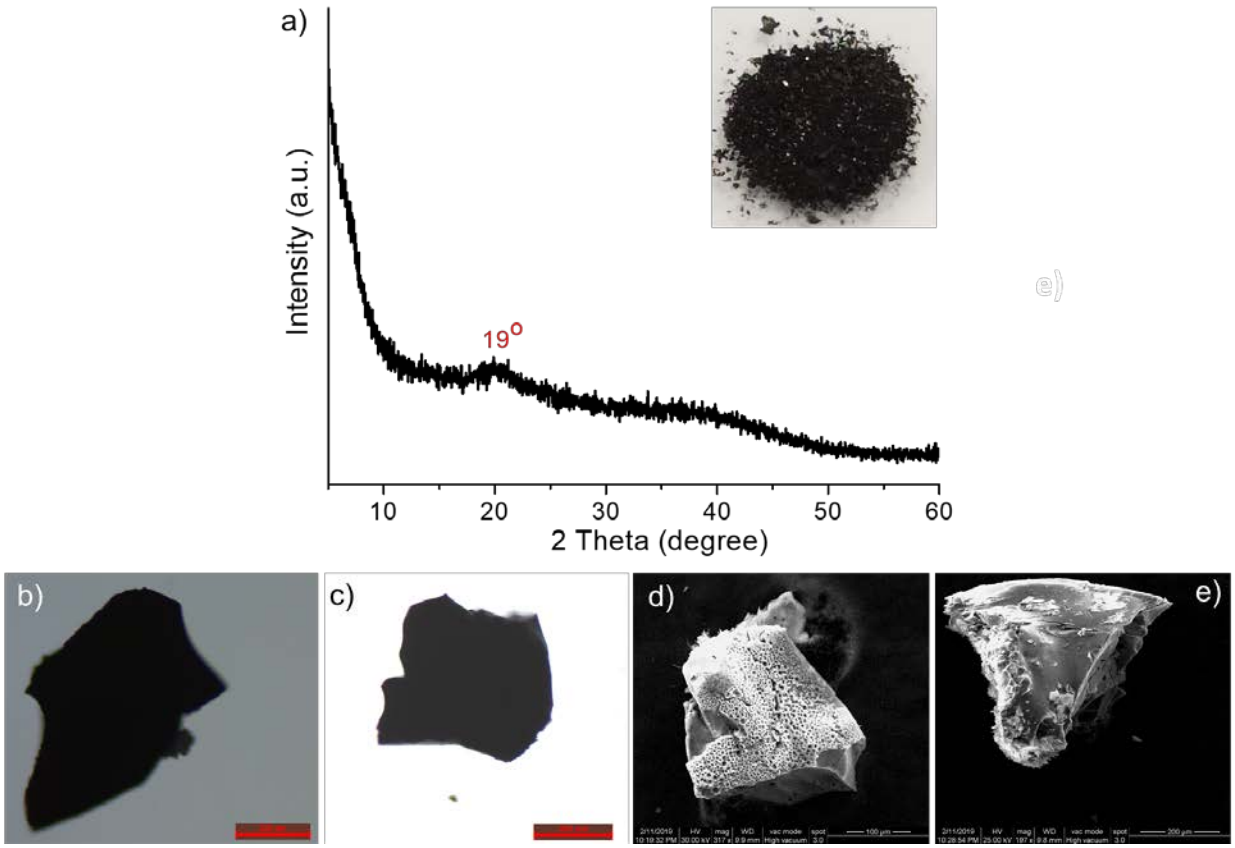

Figure S5. a) Powder XRD pattern of the Ag_{42}, which didn't show any significant diffraction peaks, indicating its weak crystallinity. Inset shows the optical image of powder of Ag_{42}. b, c) Optical microscopic images of the black color solids grown during crystallization. d, e) SEM images of the crystalline solids at different magnification.

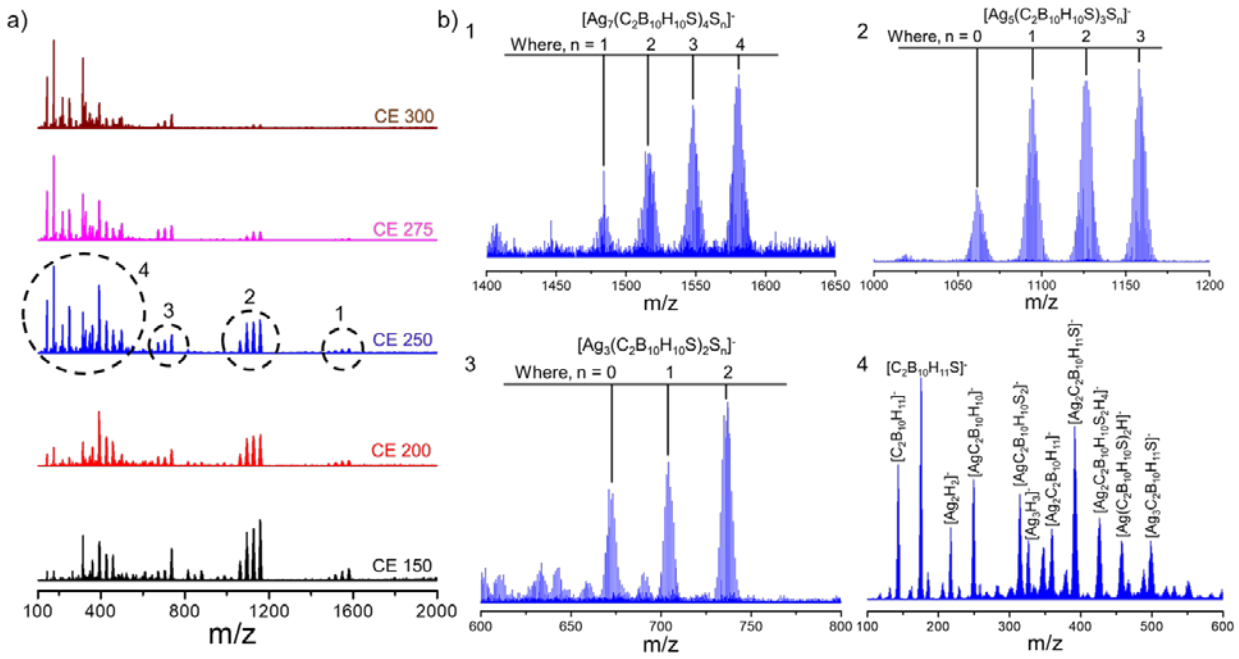

Figure S6. a) The collision energy dependent fragmentation patterns at lower mass range shows the formation of different silver thiolate species at higher collision energies. b) Expanded views of four different spectral regions having silver and carborane fragments.

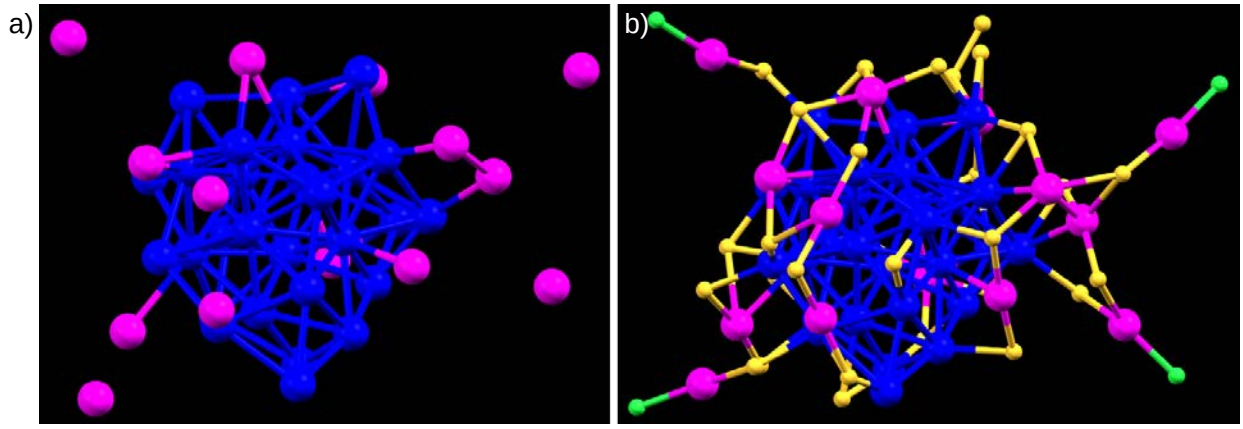

Figure S7. The DFT optimized core structure of Ag_{42}, a) the Ag_{42} core having Ag_{28} inner core, and Ag_{14} outer core, b) the same core connected with phosphorous and sulphur atoms. Ligands are removed for clarity. Atomic color codes as, blue = inner core 28 Ag atoms, pink = outer core 14 Ag atoms, yellow = sulphur, green = phosphorous.

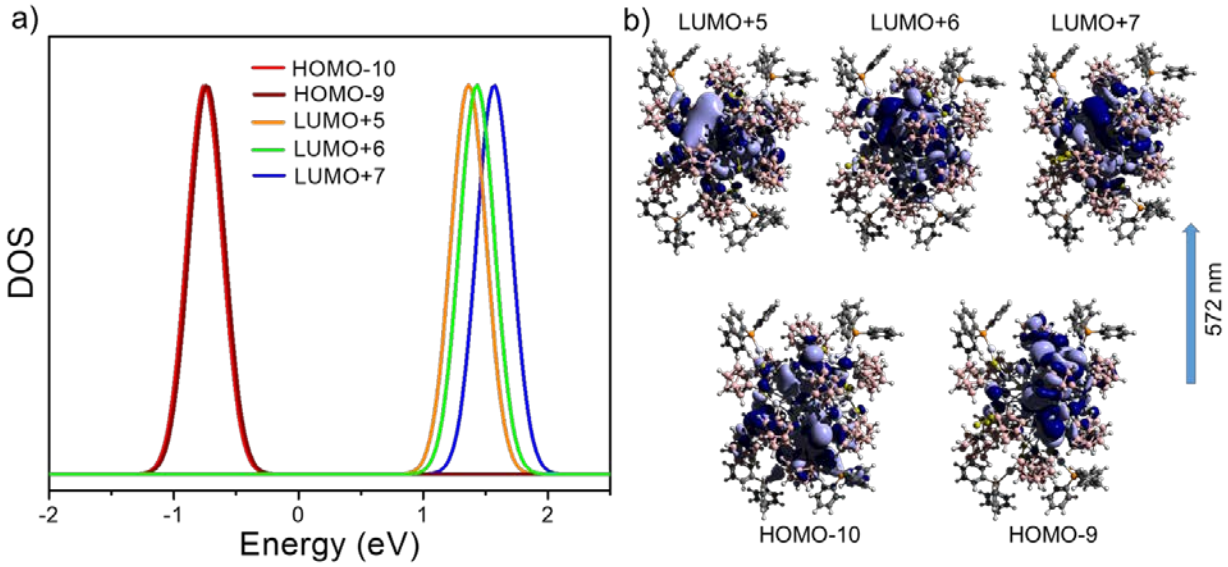

Figure S8. a) Density of states of Ag_{42} indicating the molecular orbitals contribution for the transition at 572 nm. b) Electron density plots of the respective molecular orbitals.

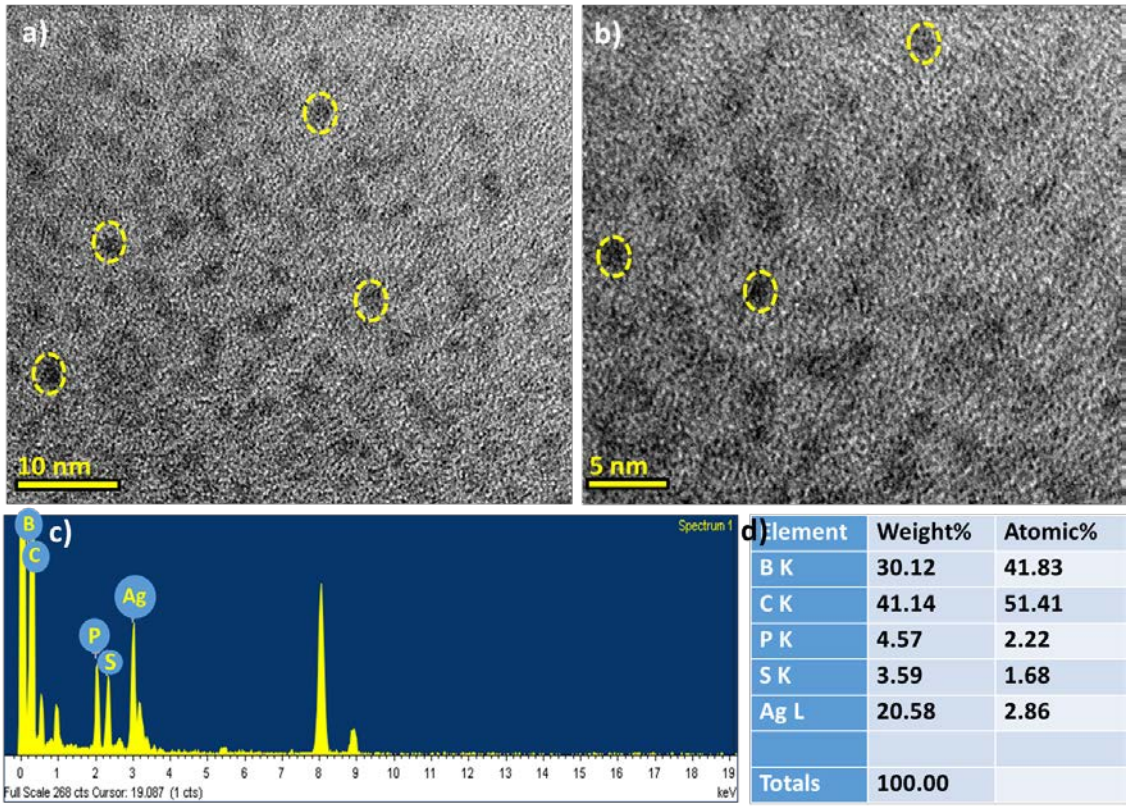

d)

Element	Weight%	Atomic%
B K	30.12	41.83
C K	41.14	51.41
P K	4.57	2.22
S K	3.59	1.68
Ag L	20.58	2.86
Totals	100.00	

Figure S9. a-b) TEM images of the Ag_{42} in different magnification. c) EDS spectrum of the nanocluster showed the existing elements. d) Atomic % and weight % of the existing elements.

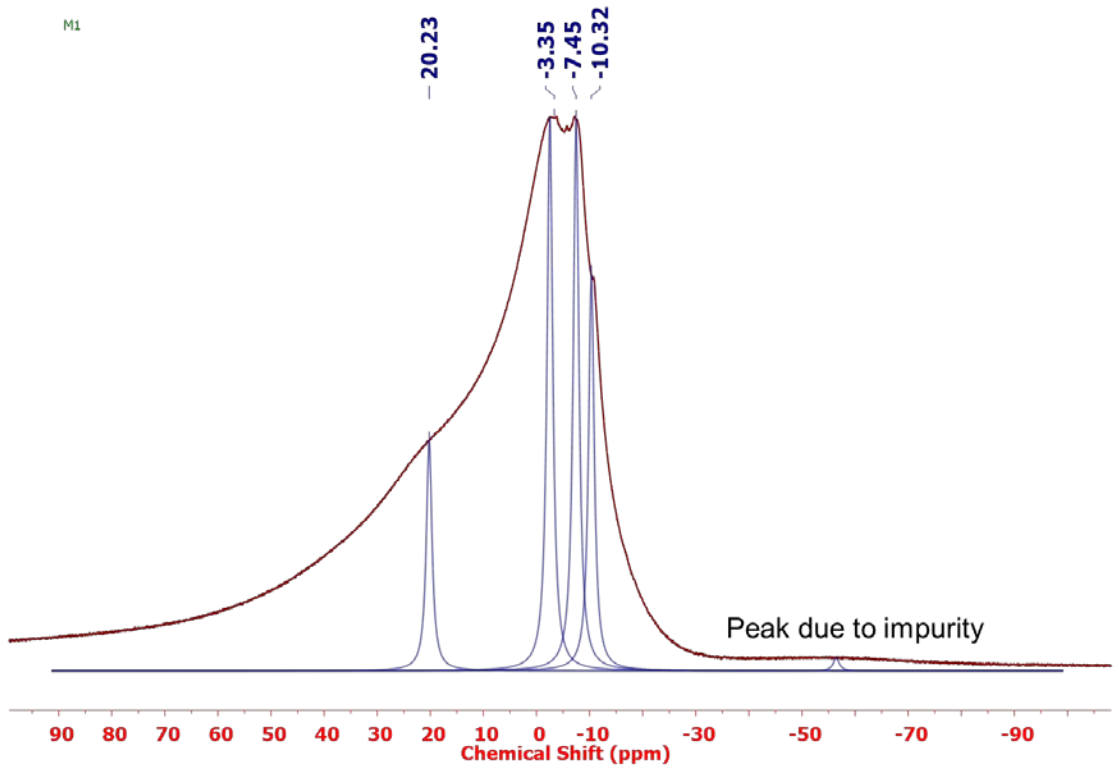

Figure S10. ^{11}B NMR spectrum of the Ag_{42} nanocluster in $CDCl_3$ solvent.

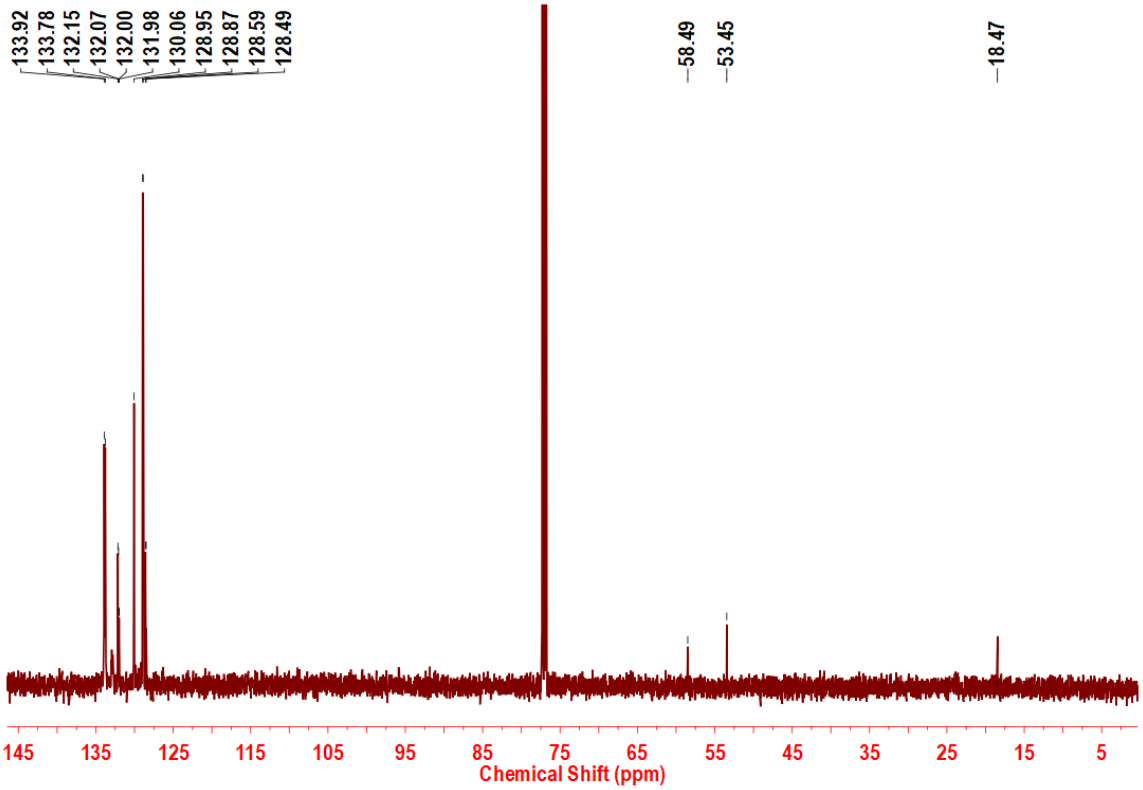

Figure S11. ^{13}C $\{^1H\}$ NMR spectrum of the Ag_{42} nanocluster in $CDCl_3$ solvent.

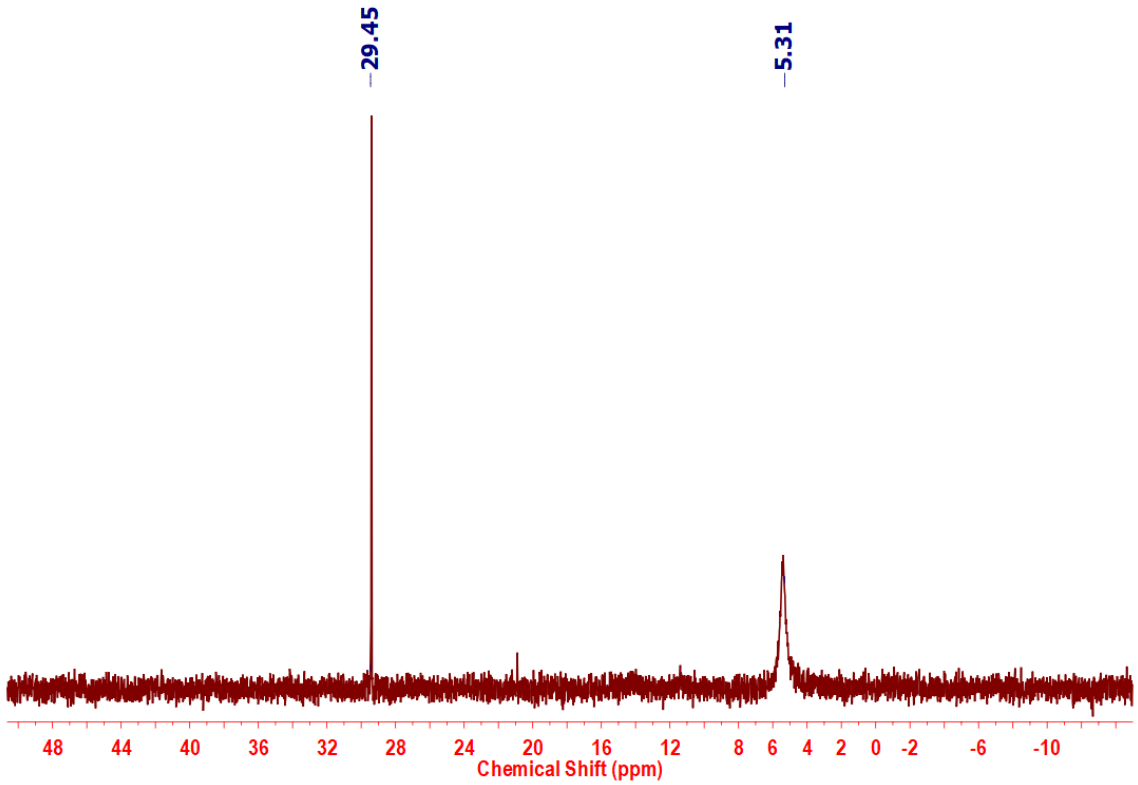

Figure S12. ^{31}P NMR spectrum of the Ag_{42} nanocluster in $CDCl_3$ solvent.

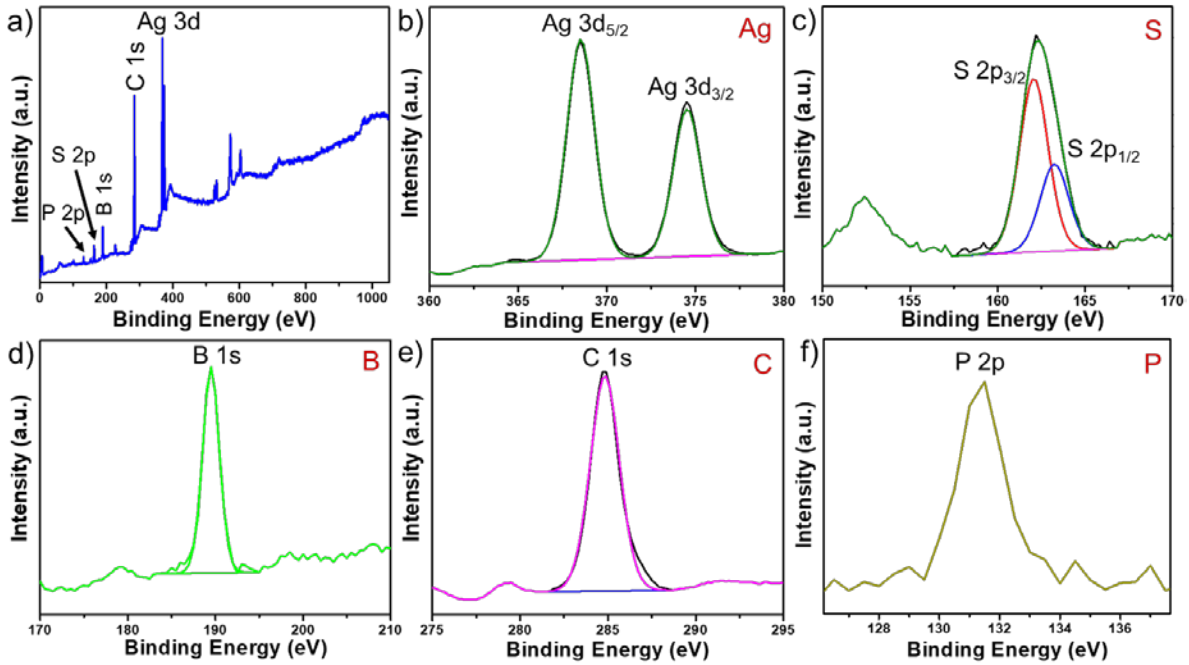

Figure S13. XPS spectra of Ag_{42}; a) XPS survey spectrum showed the signature peaks of the existing elements. Spectral fitting of b) Ag 3d region, c) S 2p region, d) B 1s region, e) C 1S region, f) P 2p region.

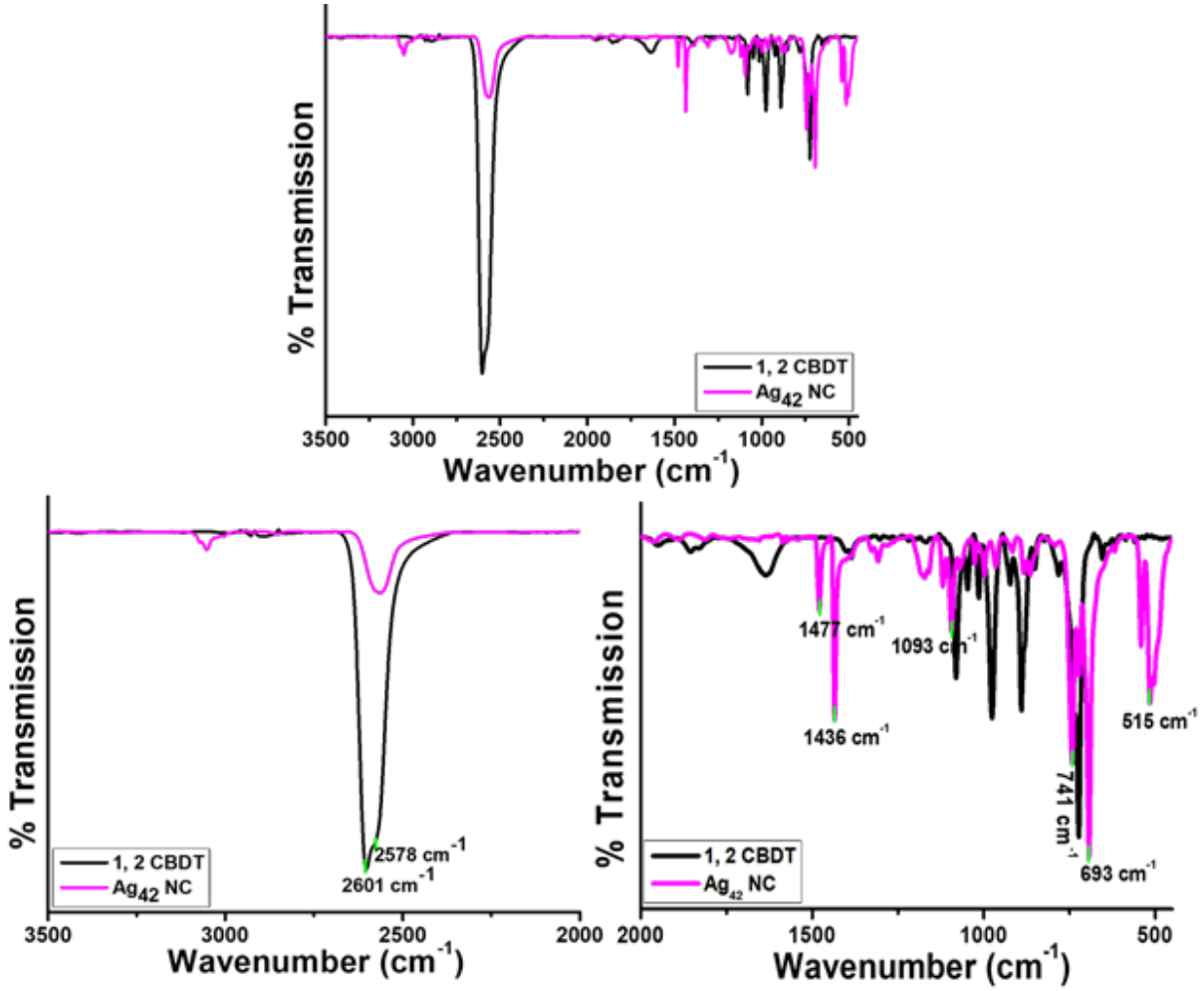

Figure S14. Combined FT-IR spectra of the *ortho*-carborane-1, 2-dithiol ligand, and Ag_{42} NC (top spectrum). Expanded view of the same spectra indicates the specific regions (bottom spectra).

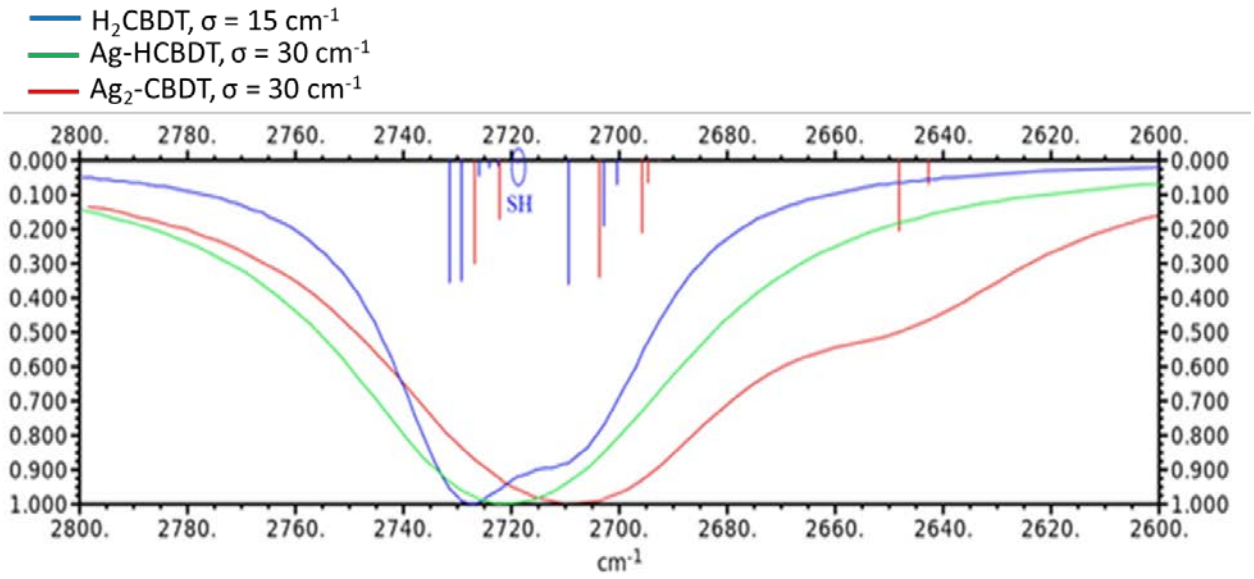

Figure S15. Calculated spectra of free CBDT (labelled as H_2CBDT) and its respective bis-silver salt Ag_2-CBDT. Circled is the area of SH vibrations.

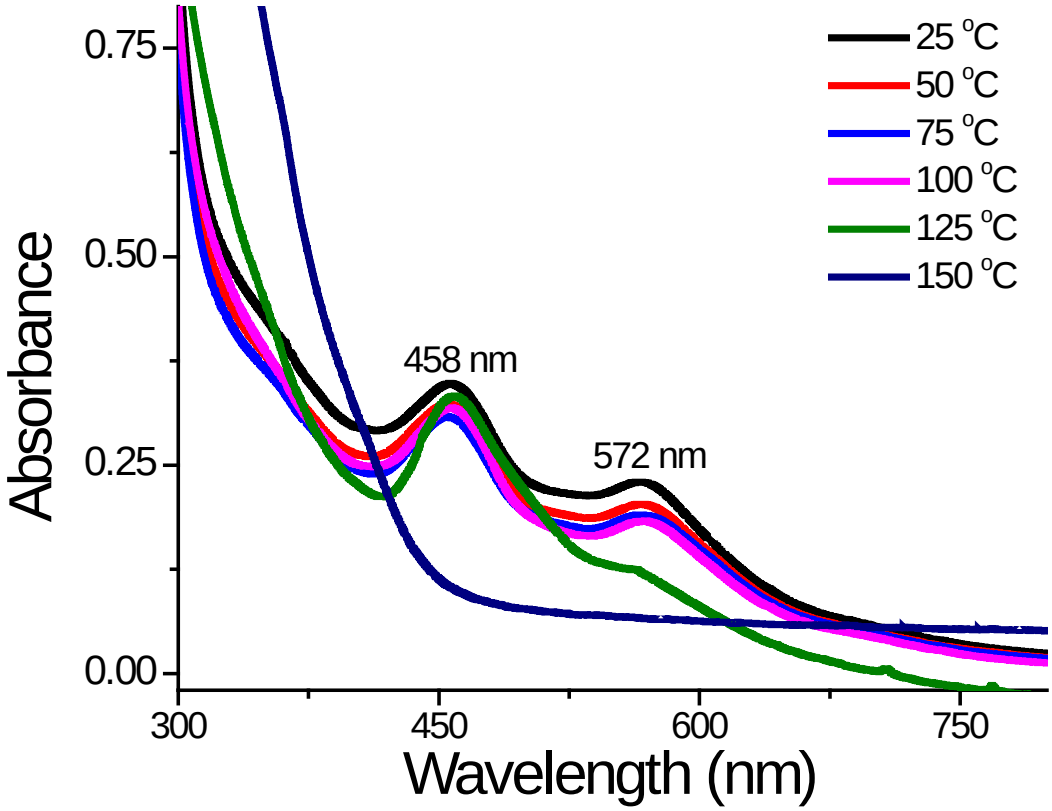

Figure S16. UV-vis absorption spectra of Ag_{42} cluster after heating at different temperatures in solid state.

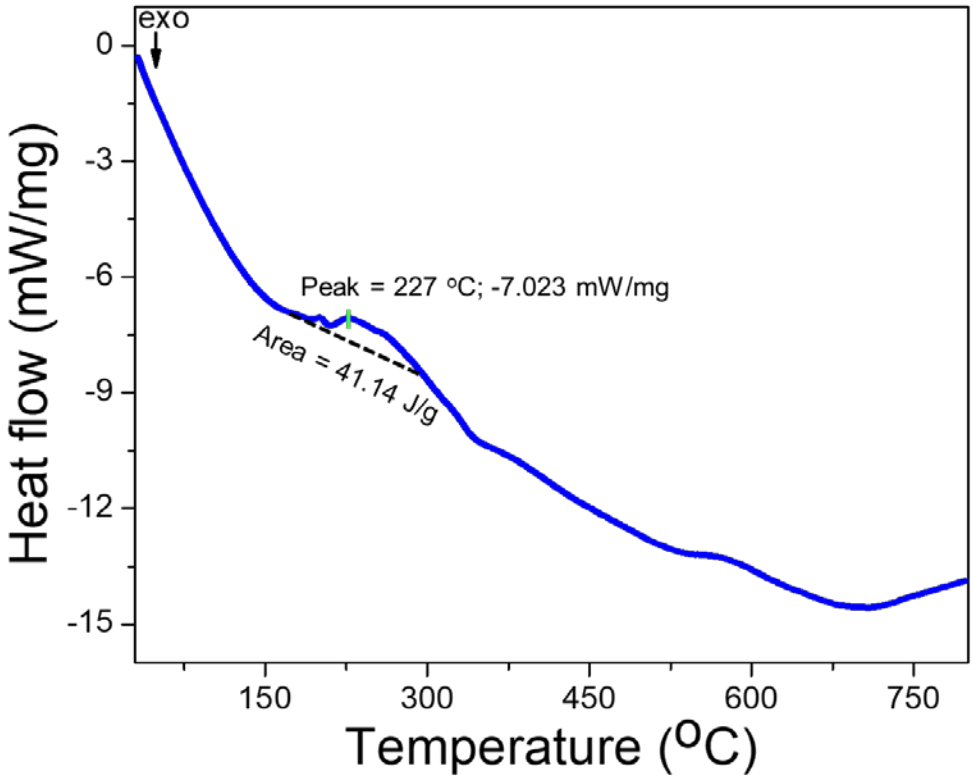

Figure S17. Differential scanning calorimetry data of Ag_{42} solid. No phase transition was observed up to 190 °C. The broad endothermic peak at 227 °C is attributed to a weak structural transformation, possibly due to ligand ordering.

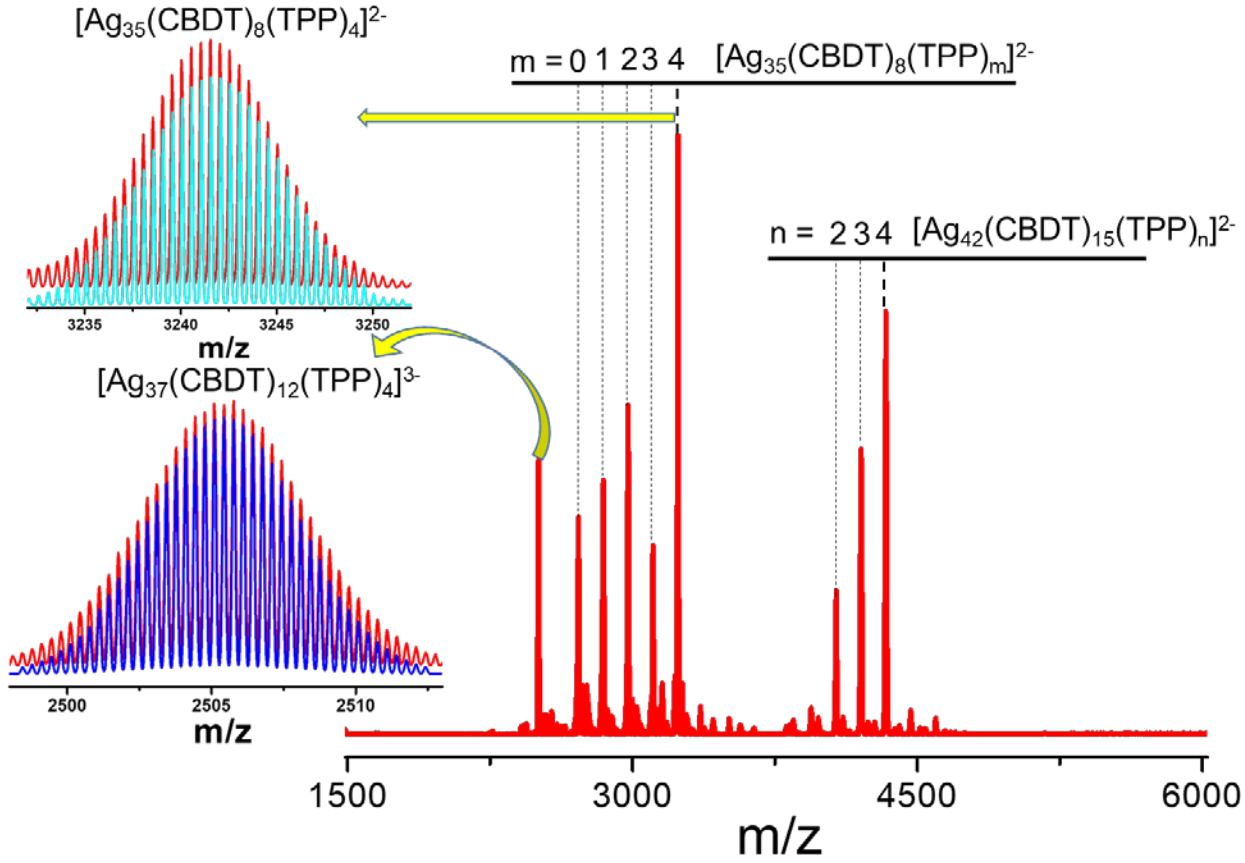

Figure S18. Negative ion-mode ESI-MS spectrum of the Int. I NCs indicating formation of $[Ag_{35}(CBDT)_8(TPP)_4]^{2-}$, and $[Ag_{37}(CBDT)_{12}(TPP)_4]^{3-}$ NCs. Inset: Exact matching of the isotopic distribution of the experimental and theoretical spectrum of the respective NCs. The subsequent TPP losses from their parent NC were observed.

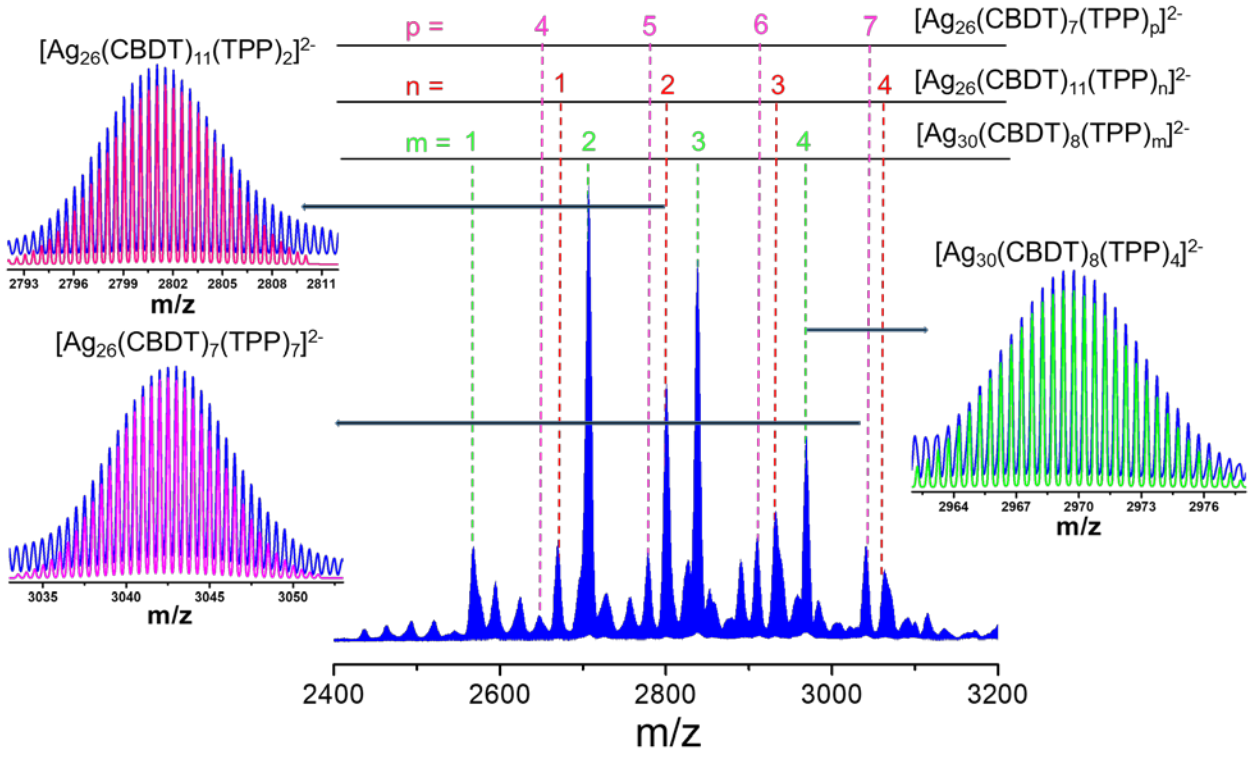

Figure S19. Negative ion-mode ESI-MS spectrum of Int. II NCs indicating the formation of $[Ag_{30}(CBDT)_8(TPP)_4]^{2-}$, $[Ag_{26}(CBDT)_{11}(TPP)_4]^{2-}$, and $[Ag_{26}(CBDT)_7(TPP)_7]^{2-}$ parent nanoclusters after 16 hr. light irradiation. Inset shows the exact matching of the isotopic distribution with the simulated spectra. The subsequent TPP losses from their parent nanoclusters were observed.

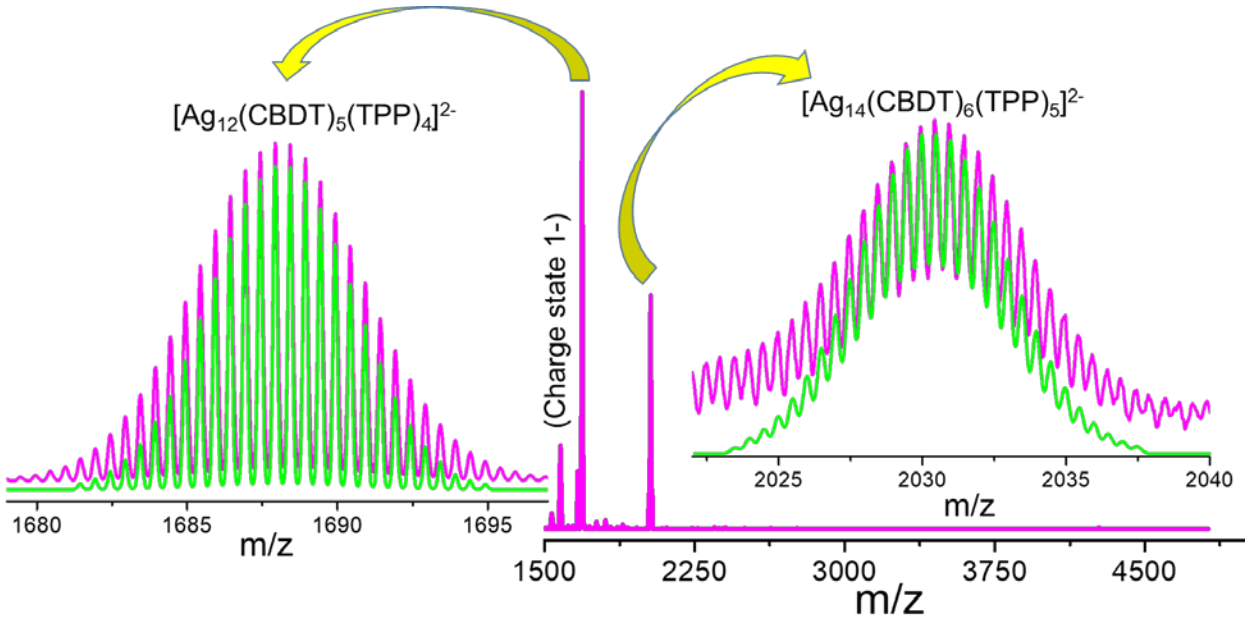

Figure S20. Negative ion-mode ESI-MS spectrum of the as synthesized Ag_{14} after 24 hr. light irradiation. $[Ag_{12}(CBDT)_5(TPP)_4]^{2-}$ peak also observed due to $[Ag_2(CBDT)(TPP)_2]$ fragment loss from the original Ag_{14} NC. Inset shows the exact matching of the isotopic distribution with the respective theoretical spectrum.

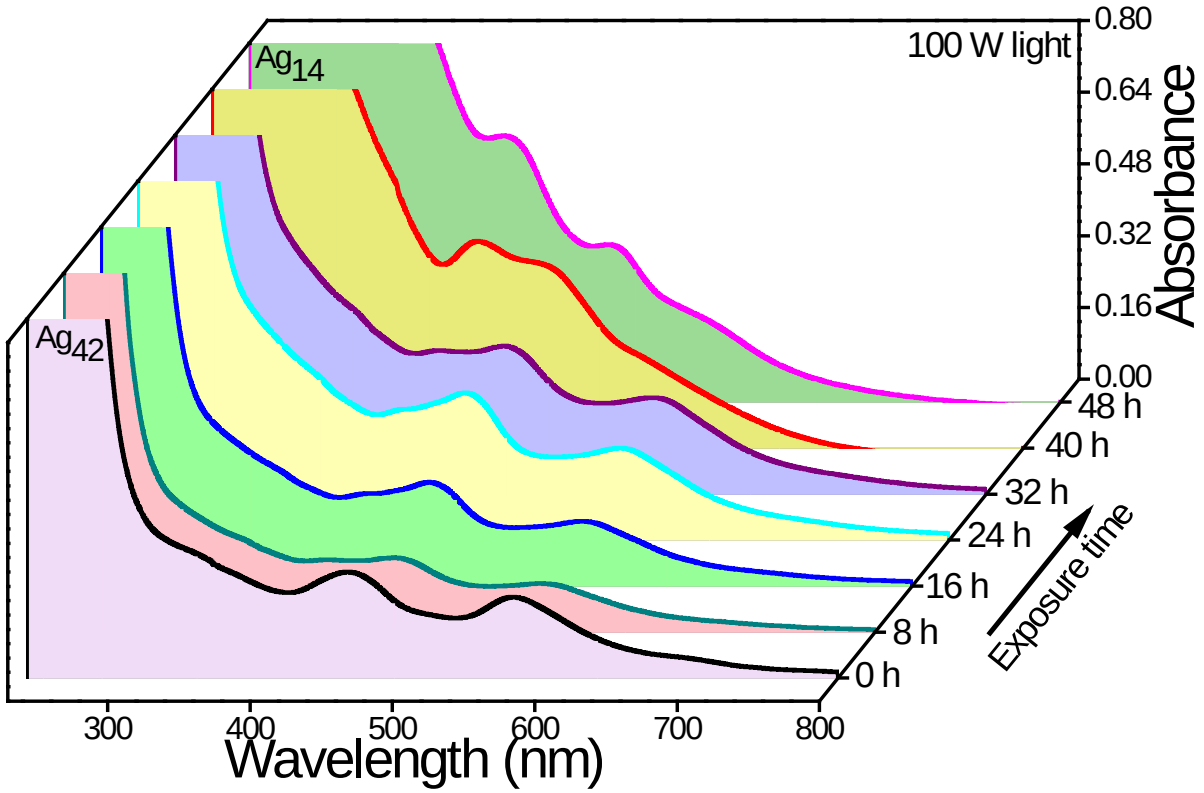

Figure S21. Time-dependent interconversion of Ag_{42} to Ag_{14} at an irradiation power of 100 W.

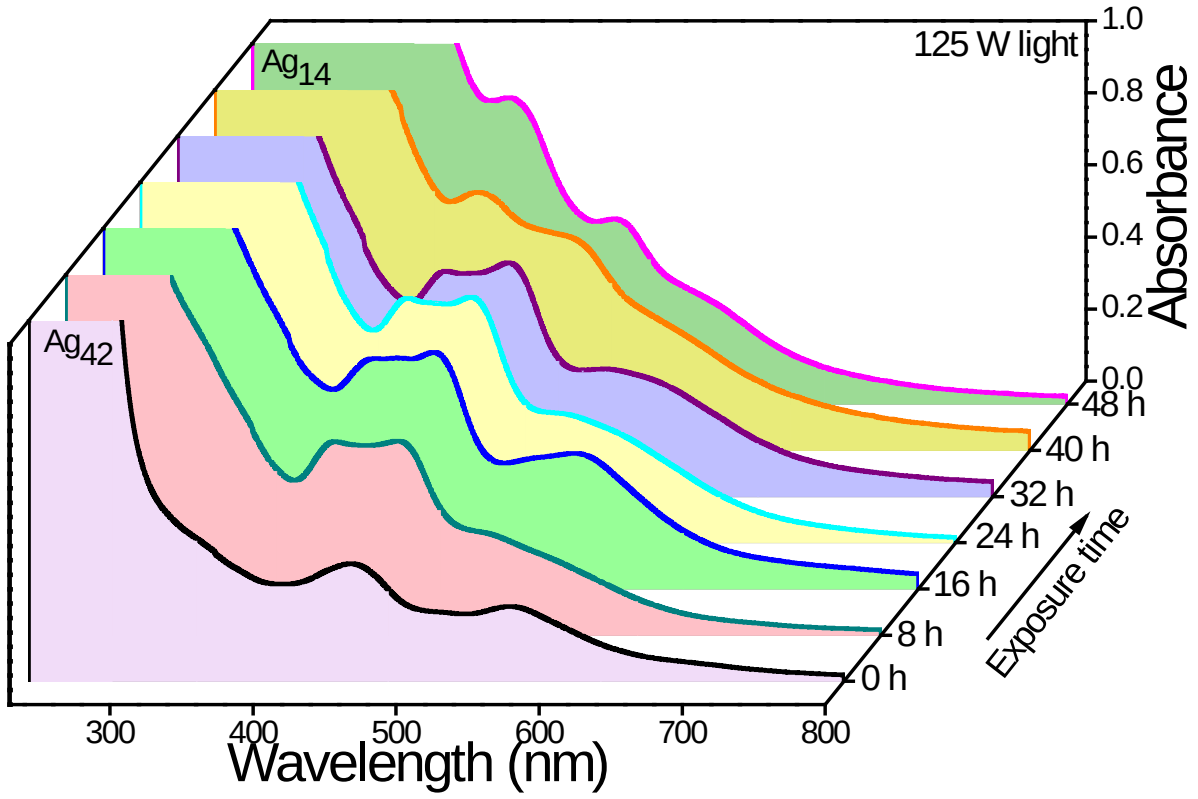

Figure S22. Time-dependent interconversion of Ag_{42} to Ag_{14} at an irradiation power of 125 W.

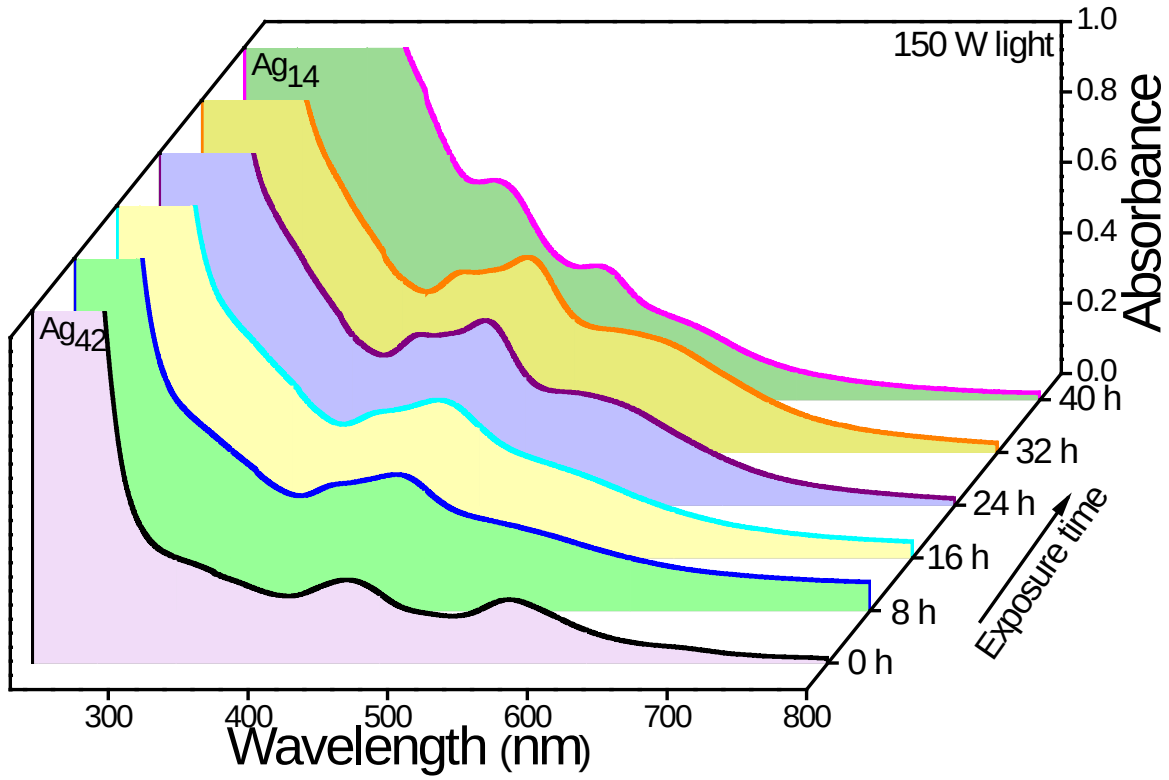

Figure S23. Time-dependent interconversion of Ag_{42} to Ag_{14} at an irradiation power of 150 W.

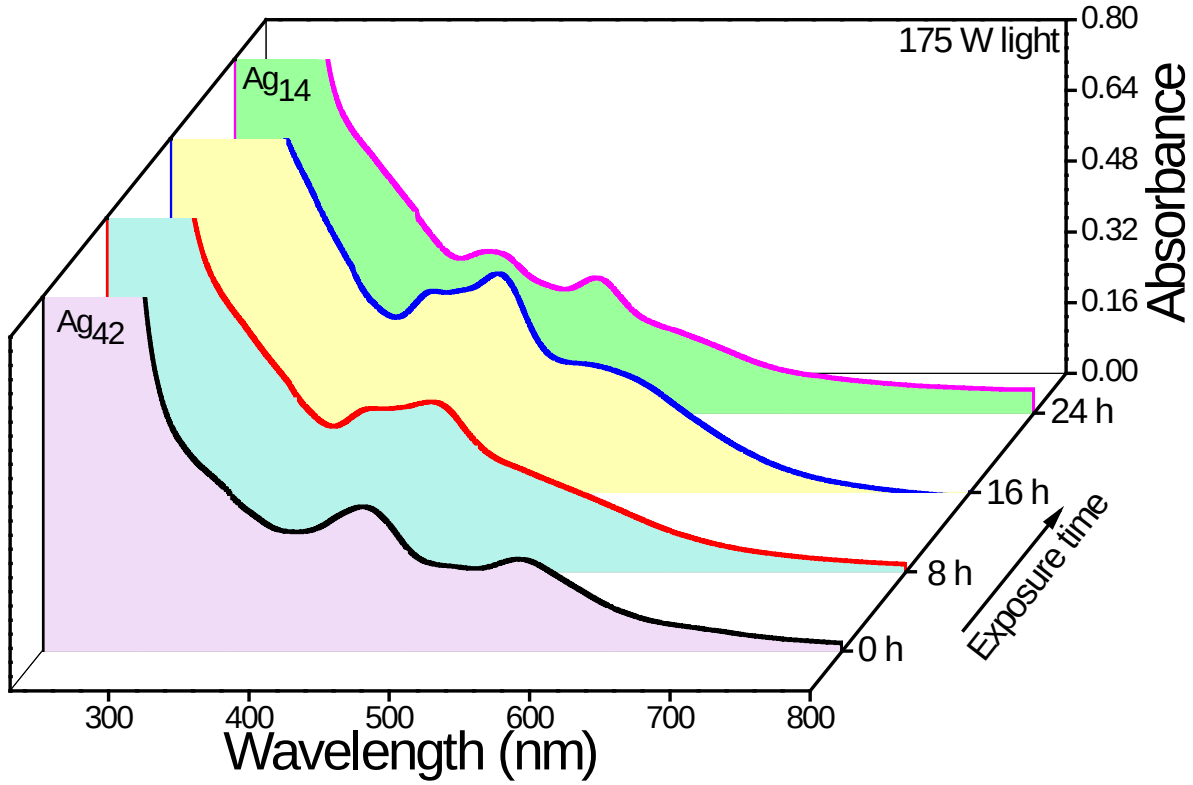

Figure S24. Time-dependent interconversion of Ag_{42} to Ag_{14} at an irradiation power of 175 W.

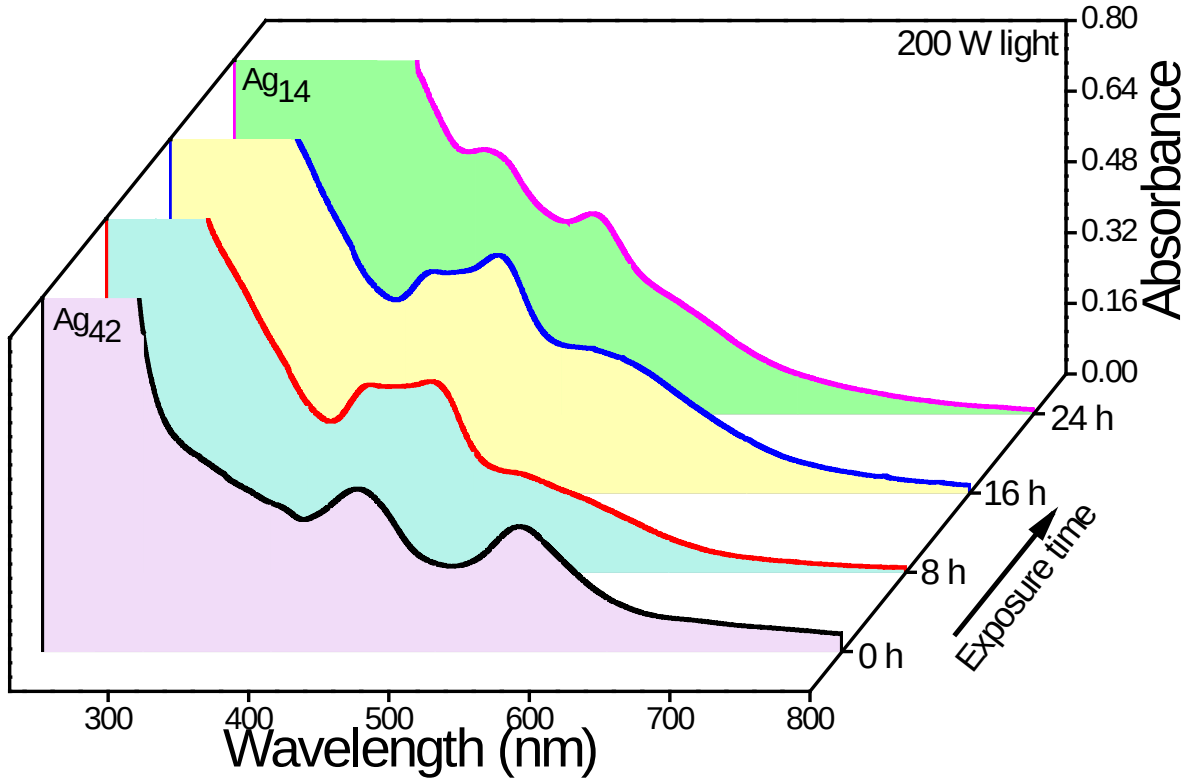

Figure S25. Time-dependent interconversion of Ag_{42} to Ag_{14} at an irradiation power of 200 W.

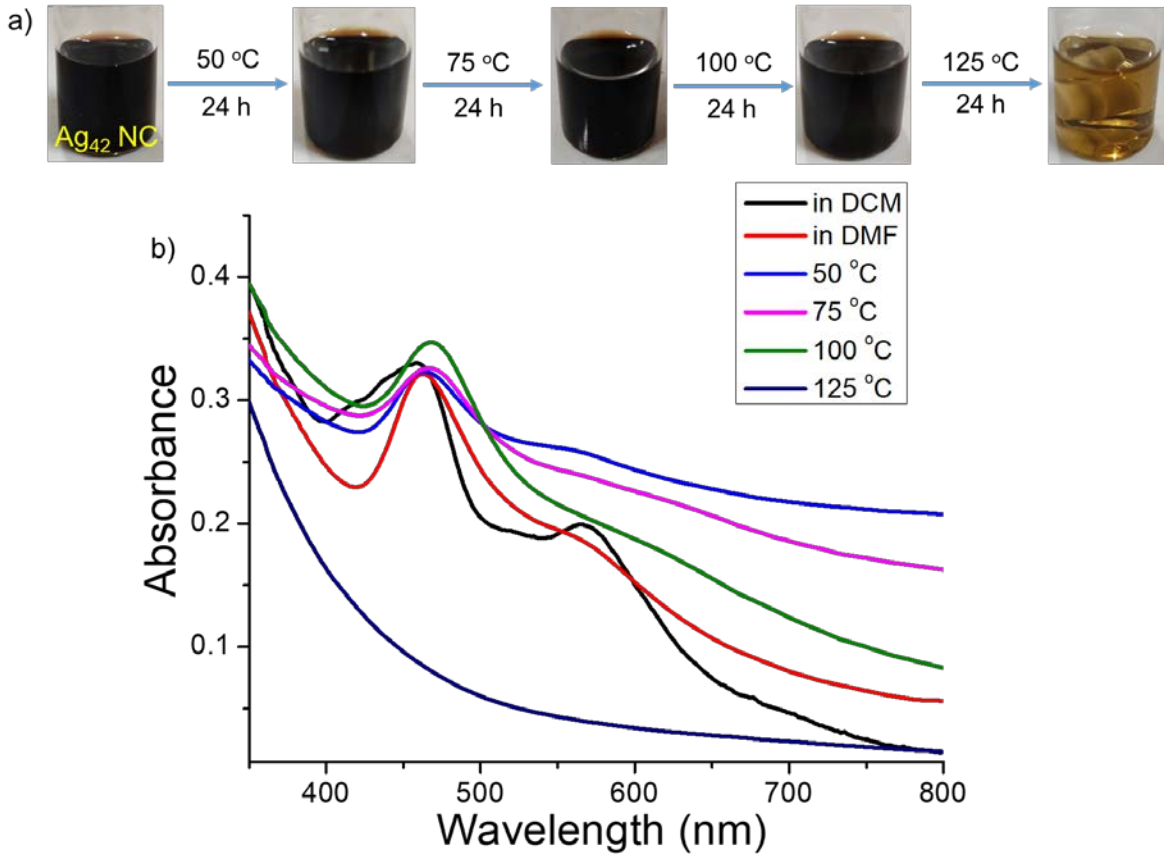

Figure S26. a) Photographs of the Ag_{42} in DMF during the heating of different temperatures, b) UV-vis absorption spectra were recorded for heating at above mentioned temperatures, which showed its stability up to 100 °C.

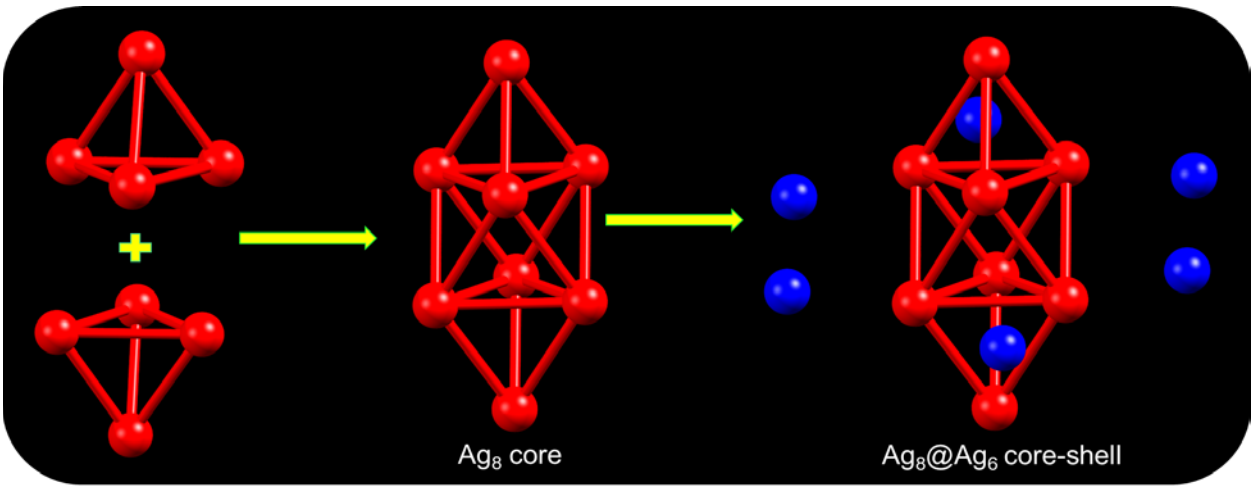

Figure S27. Atomic packing of the Ag_{14} as Ag_8 bicapped trigonal antiprism core, and Ag_6 surface silver atoms. All of the atoms are silver here. Red atoms indicate the inner Ag_8 core, blue atoms are for the outer six silver atoms.

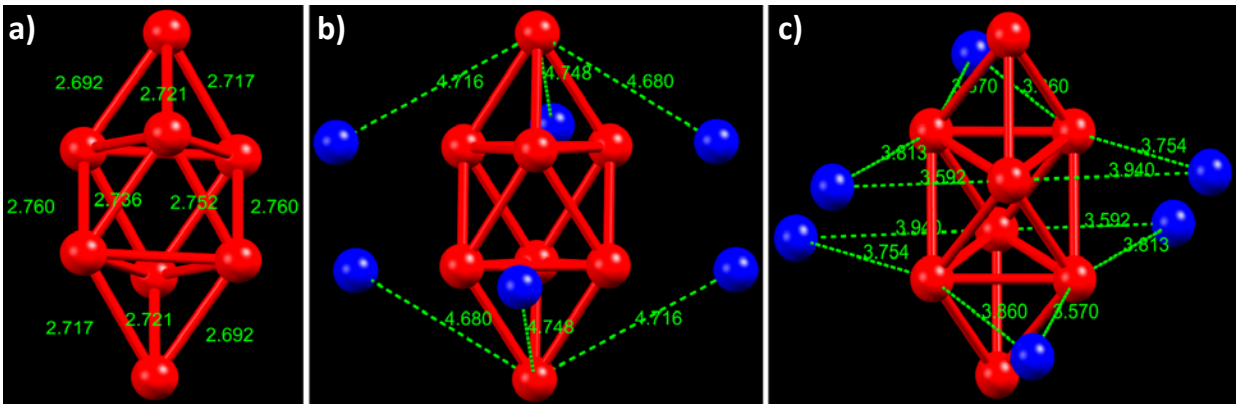

Figure S28. a) Interatomic Ag-Ag distances within Ag_8 bicapped trigonal antiprism core, b-c) interatomic distance of outer 6 Ag atoms from their nearest Ag atoms. All of the atoms are silver here.

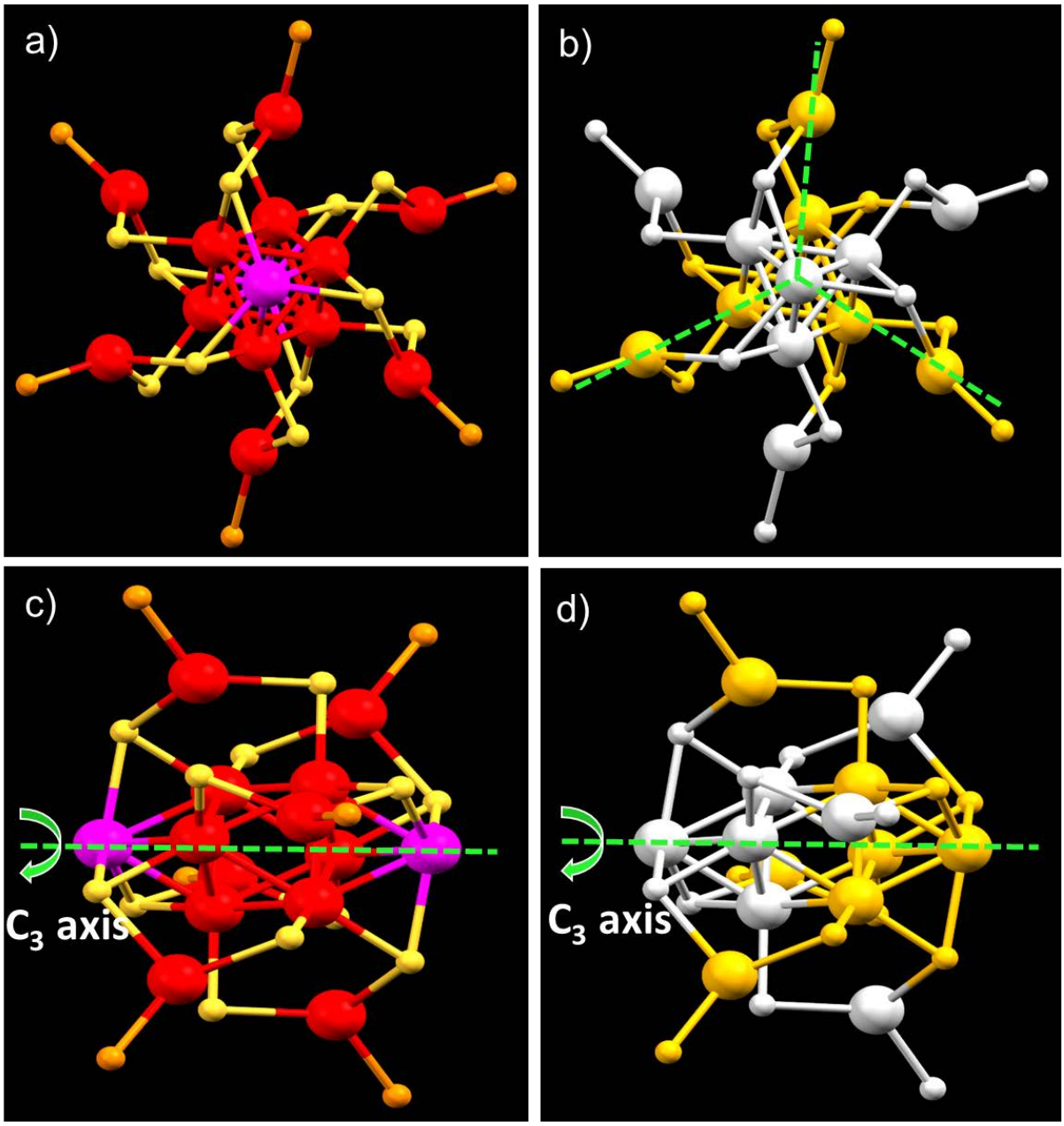

Figure S29. a-d) Single crystal structure of Ag_{14} core without CBDT, and TPP ligands with C_3 axial symmetry in a different orientation, a, c) atomic color codes as red, pink = silver, yellow = sulphur, brown = phosphorous, b, d) the same atomic arrangements with symmetry oriented colors in ball and stick model.

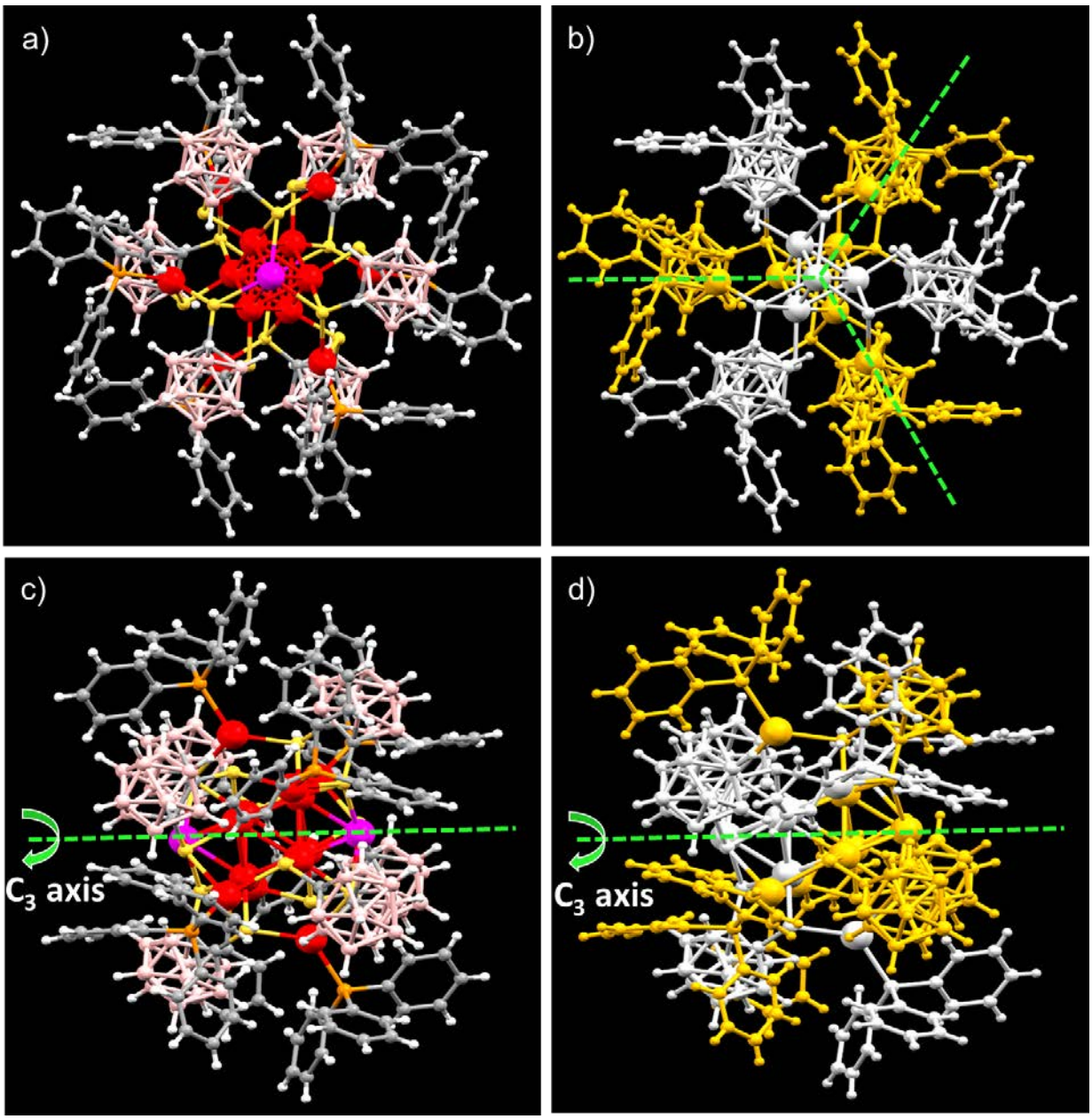

Figure S30. a-d) Full structure of the Ag_{14} having C_3 axial symmetry from two different orientation (a, c atoms are in their respective colors; b, d symmetry colors).

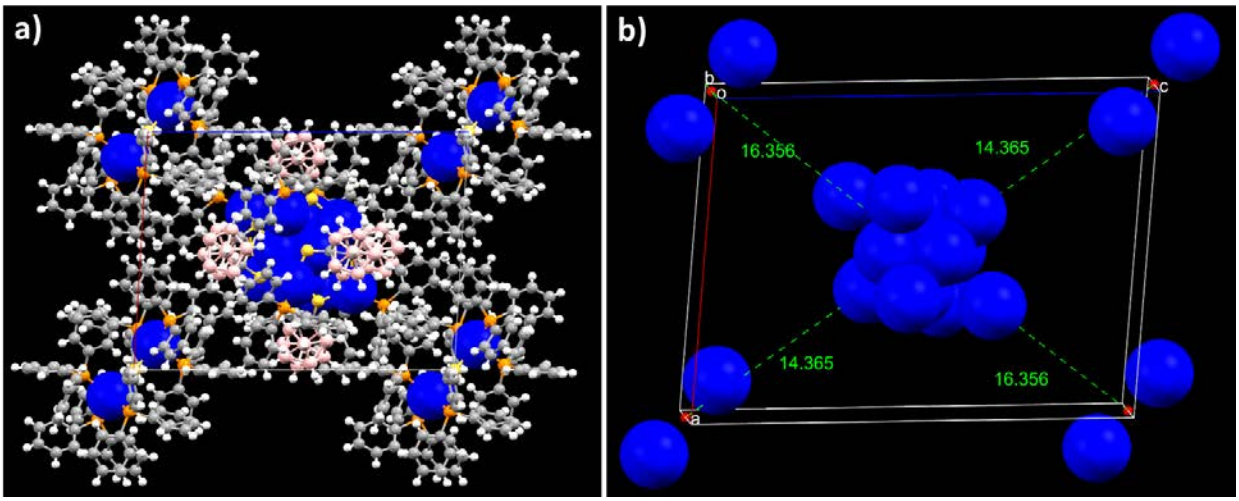

Figure S31. a) Full structure molecular packing of the Ag_{14} shows four $[Ag_2S(TPP)_6]$ units packed surrounding the Ag_{14}, b) distance between the centroids of four $[Ag_2S(TPP)_6]$ fragments from the centroids of Ag_{14} core.

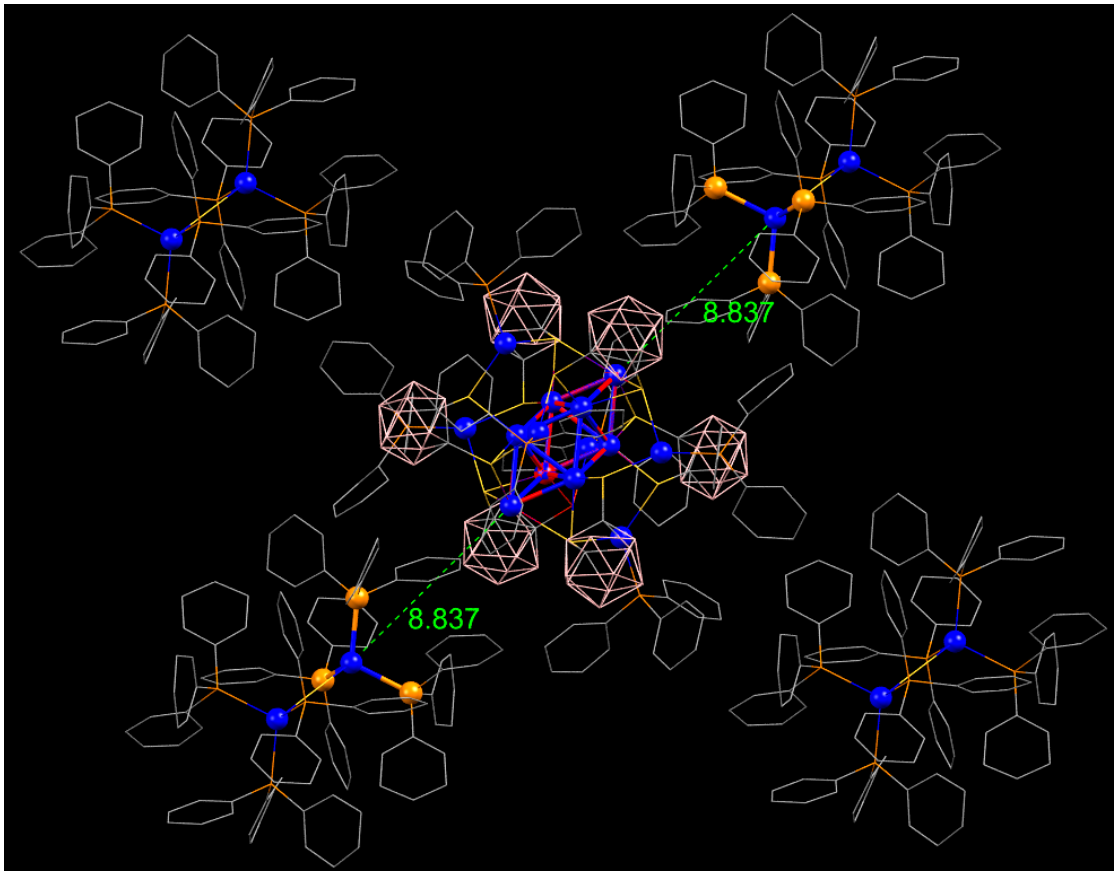

Figure S32. Single-crystal molecular packing of the Ag_{14} shows two capped silver atoms on the bicapped trigonal antiprism Ag_{14} core was shielded by the nearest TPP unit of $[Ag_2S(TPP)_6]$ (hydrogen atoms are removed for clarity).

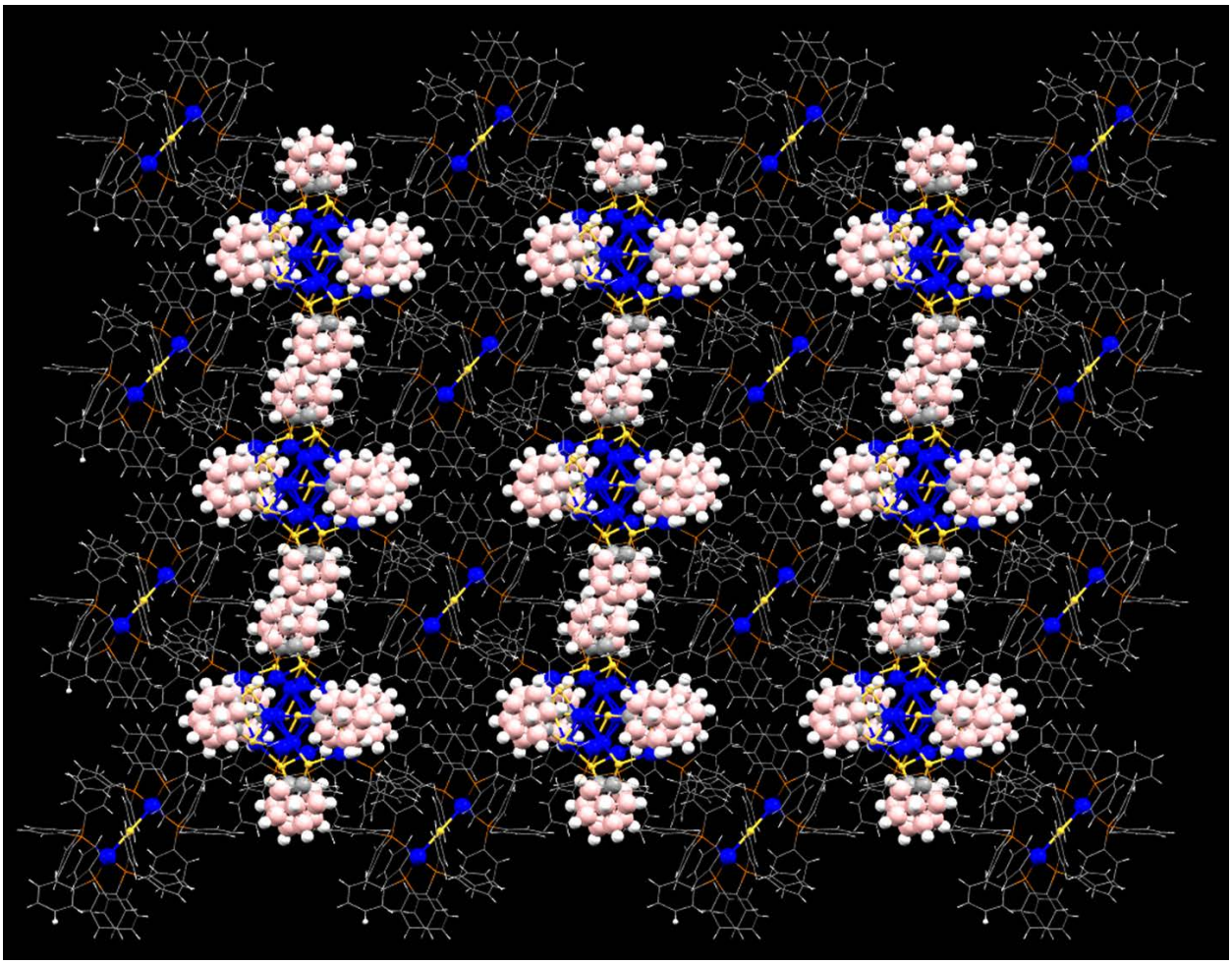

Figure S33. Extended molecular packing of the same NC showed repeating lamellar packing of $[Ag_{14}(CBDT)_6(TPP)_6]$ and $[Ag_2S(TPP)_6]$ units.

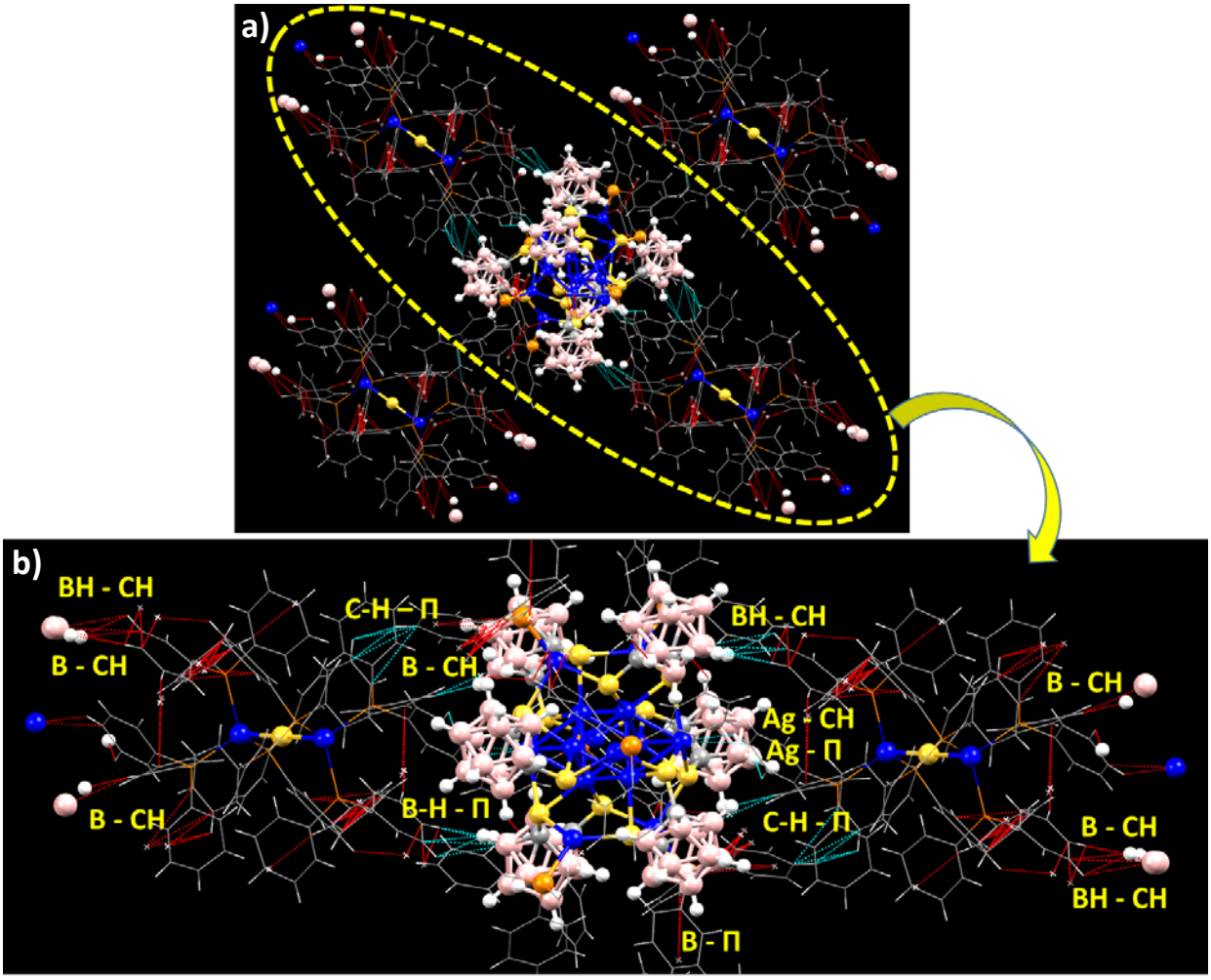

Figure S34. a-b) Intercluster packing due to different intermolecular interaction such as CH-π, BH- π, B-CH, BH-CH, Ag- π, Ag-CH, B-π of Ag_{14} with $[Ag_2S(TPP)_6]$ unit.

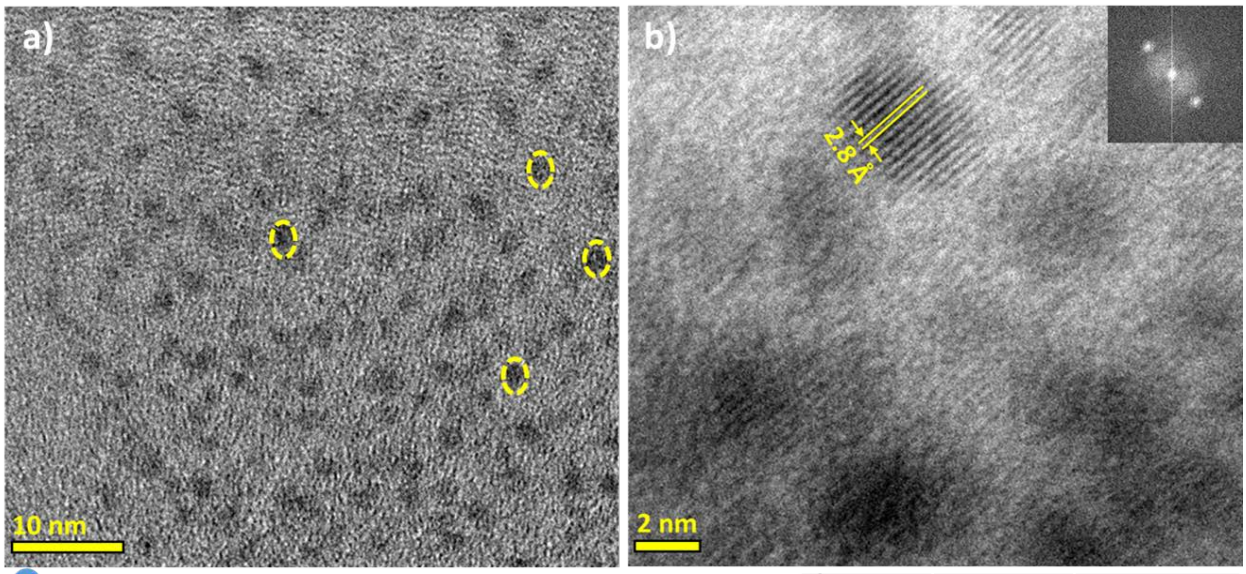

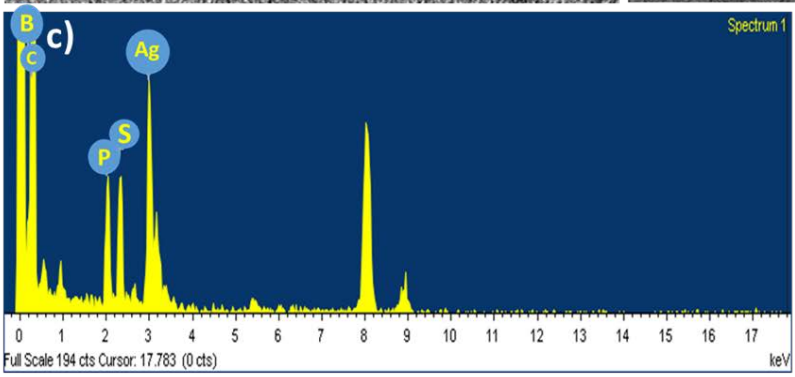

d)

Element	Weight%	Atomic%
B K	30.59	38.86
C K	49.56	56.67
P K	3.47	1.54
S K	2.80	1.20
Ag L	13.59	1.73
Totals	100.00	

Figure S35. a) TEM image of the Ag_{14}, b) HRTEM image of the NCs having lattice spacing of 2.8 Å after 5 min beam irradiation, c-d) EDS spectrum of the NC with the quantification of the respective elements.

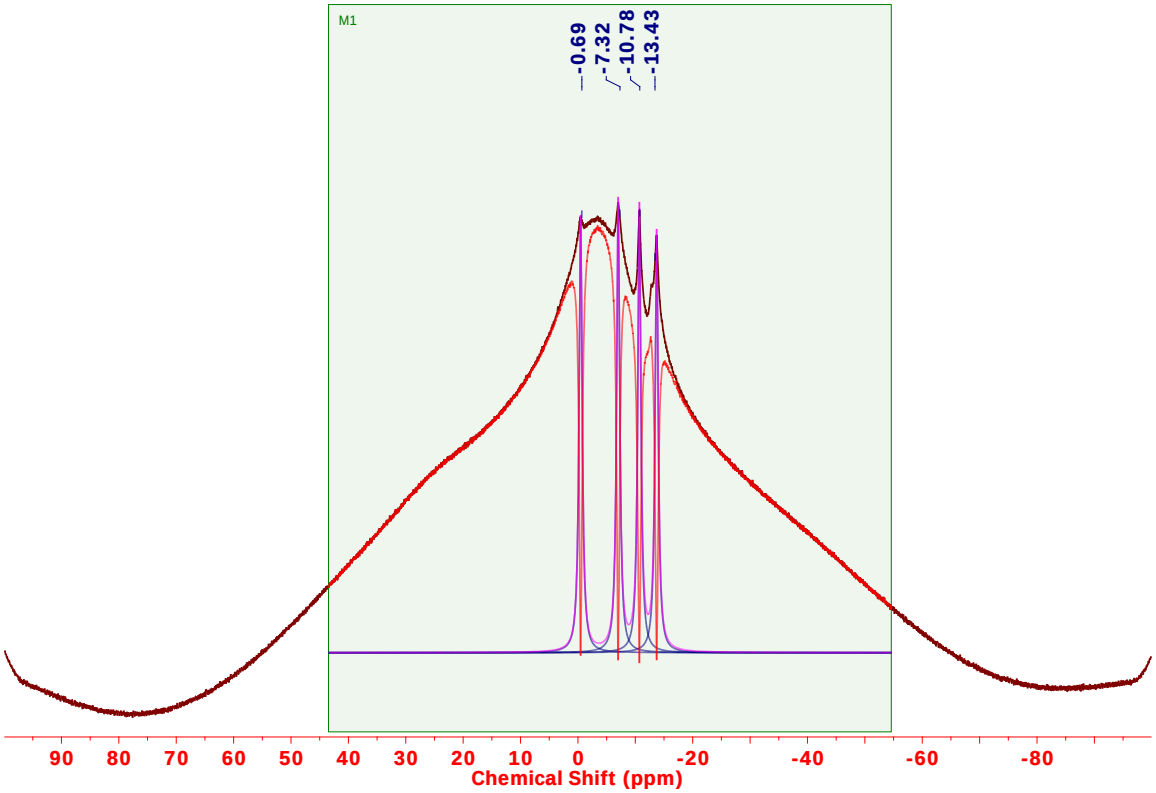

Figure S36. ^{11}B NMR spectrum of the Ag_{14} nanocluster in $CDCl_3$ solvent.

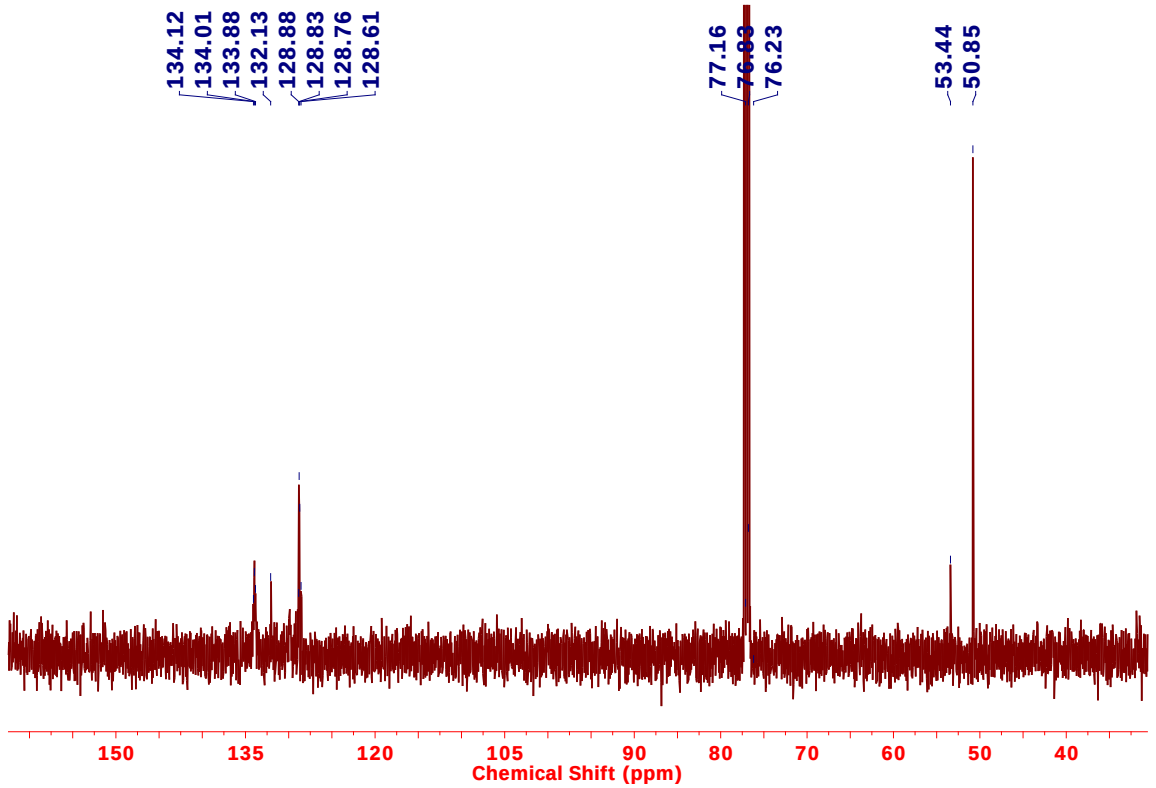

Figure S37. ^{13}C {^{1}H} NMR spectrum of the Ag_{14} nanocluster in $CDCl_3$ solvent.

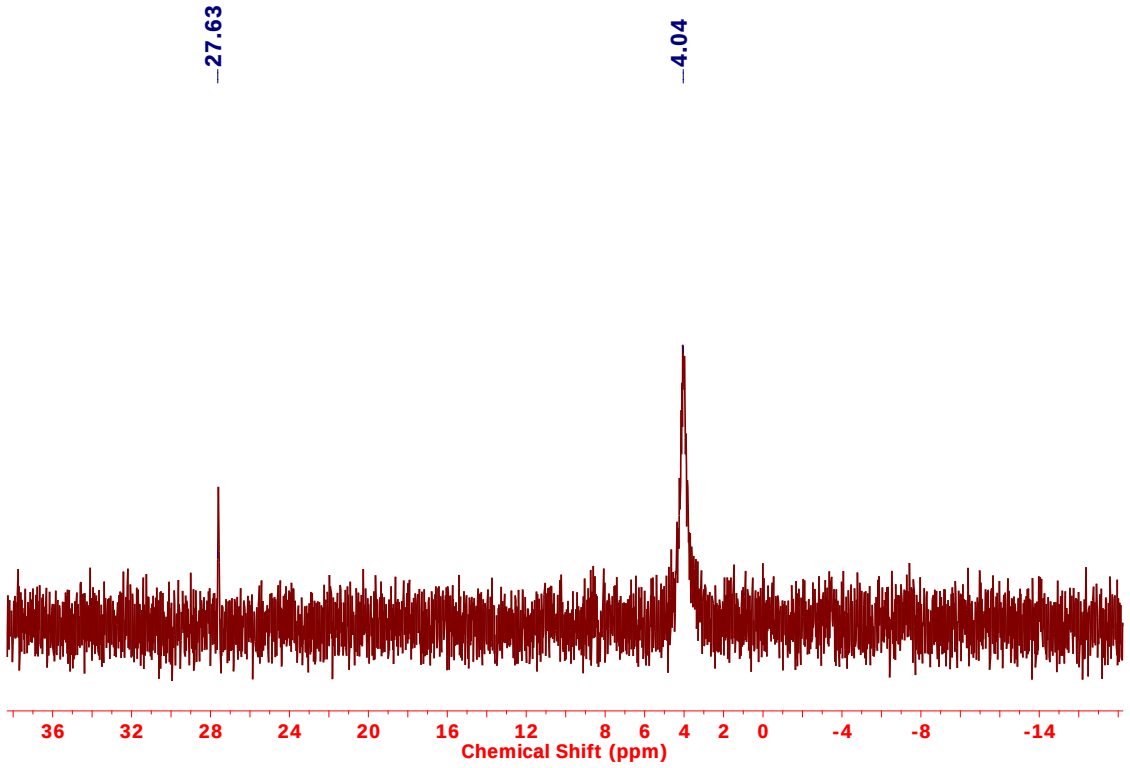

Figure S38. ^{31}P NMR spectrum of the Ag_{14} nanocluster in $CDCl_3$ solvent.

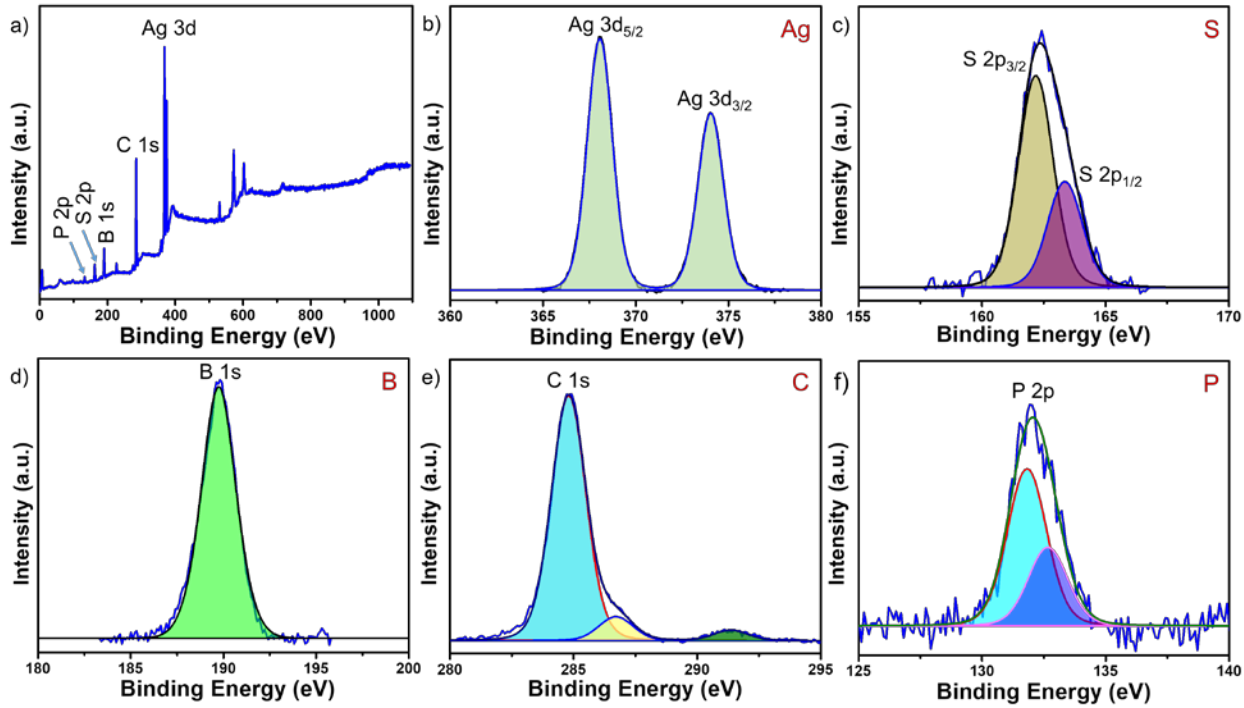

Figure S39. XPS spectra of Ag_{14}; a) XPS survey spectrum showed the signature peaks of existing elements. Spectral fitting of b) Ag 3d region, c) C 1S region, d) S 2p region, e) B 1S region, f) P 2p region.

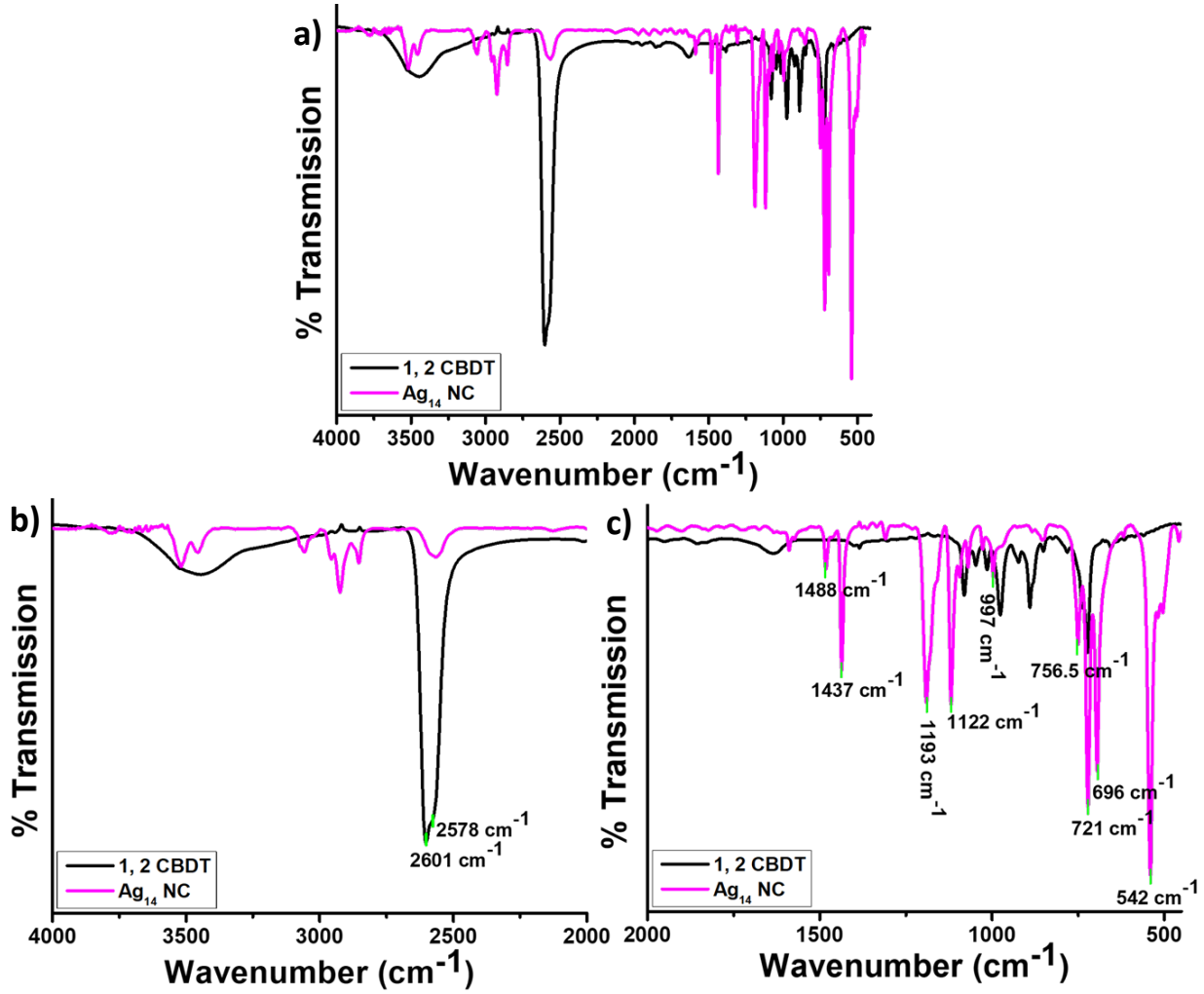

Figure S40. a) Combined FT-IR spectra of the *ortho*-carborane-1, 2-dithiol ligand, and Ag_{14} NC, b, and c) expanded view of the same spectra with peak assignments.

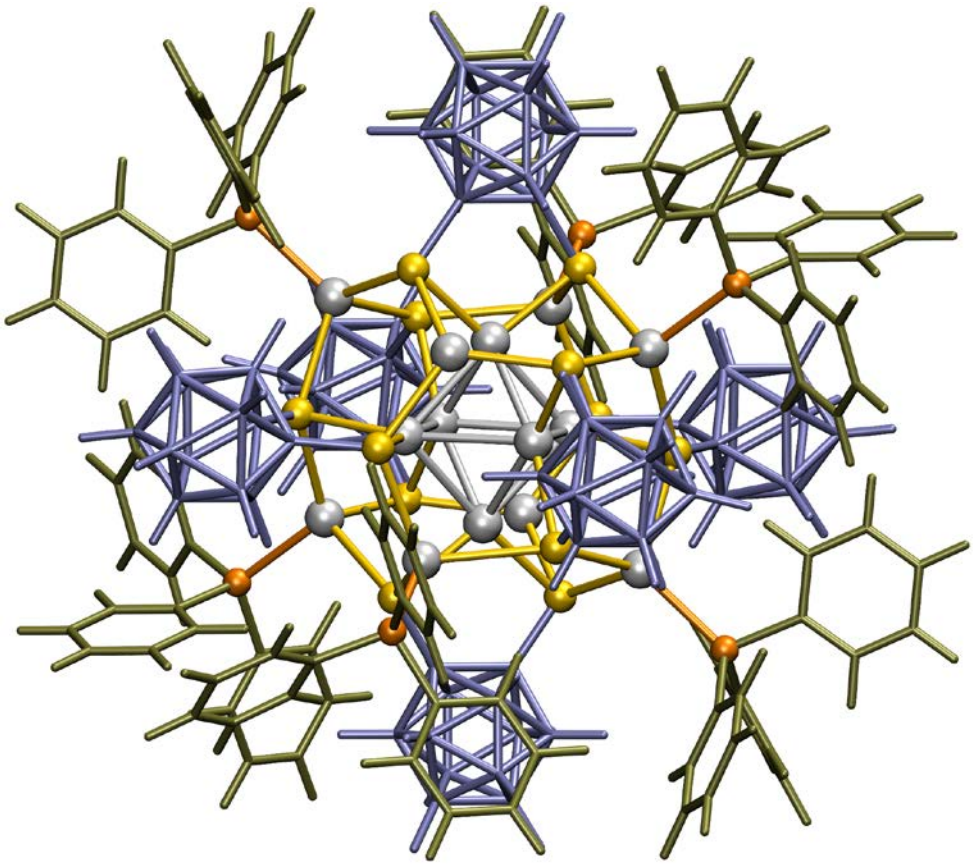

Figure S41. The DFT optimized structure of the Ag_{14} with all ligands; (color code of the atoms, grey: silver, yellow: sulphur, orange: phosphorous, blue: carborane, brown: phenyl).

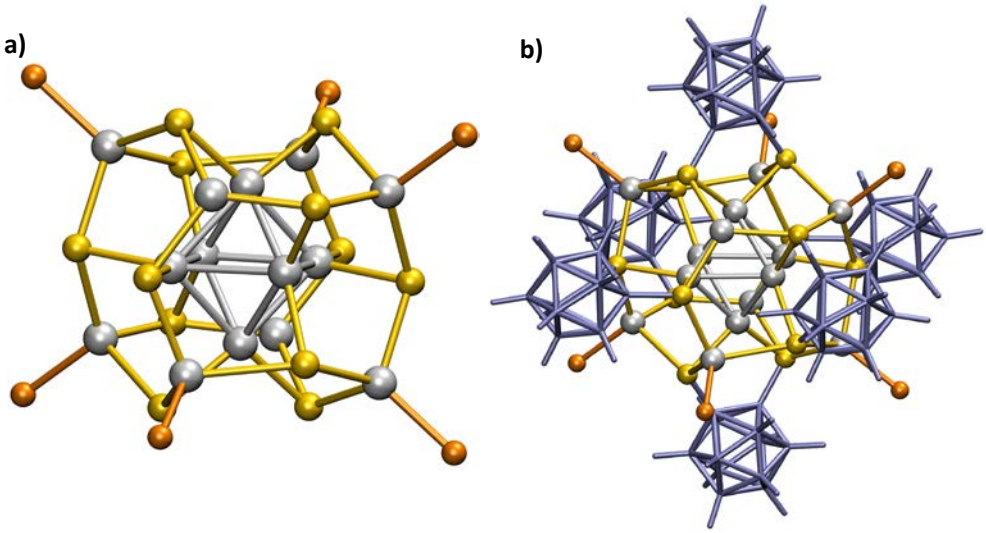

Figure S42. The DFT optimized relaxed structure of Ag_{14} a) without CBDT ligands b) with CBDT ligands. (Color code of the atoms, grey: silver, yellow: sulphur, orange: TPP, blue: carborane).

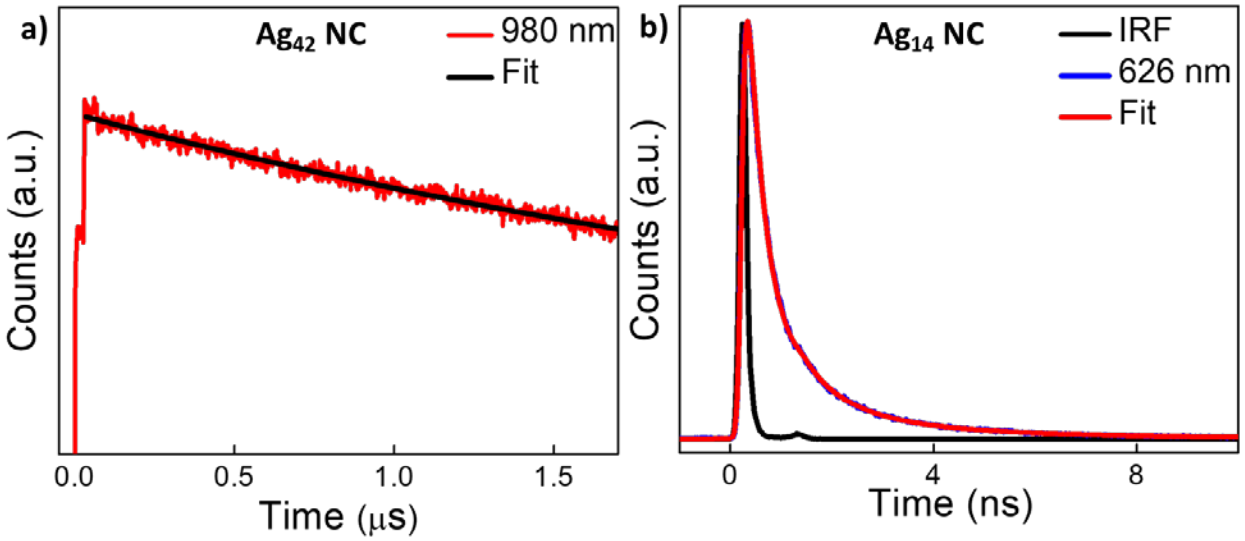

Figure S43. TCSPC data of a) lifetime decay of >1.5 μs for NIR emissive peak (980 nm) of Ag_{42} and b) lifetime decay of 550 ps corresponding to the red emissive peak (626 nm) of Ag_{14}.

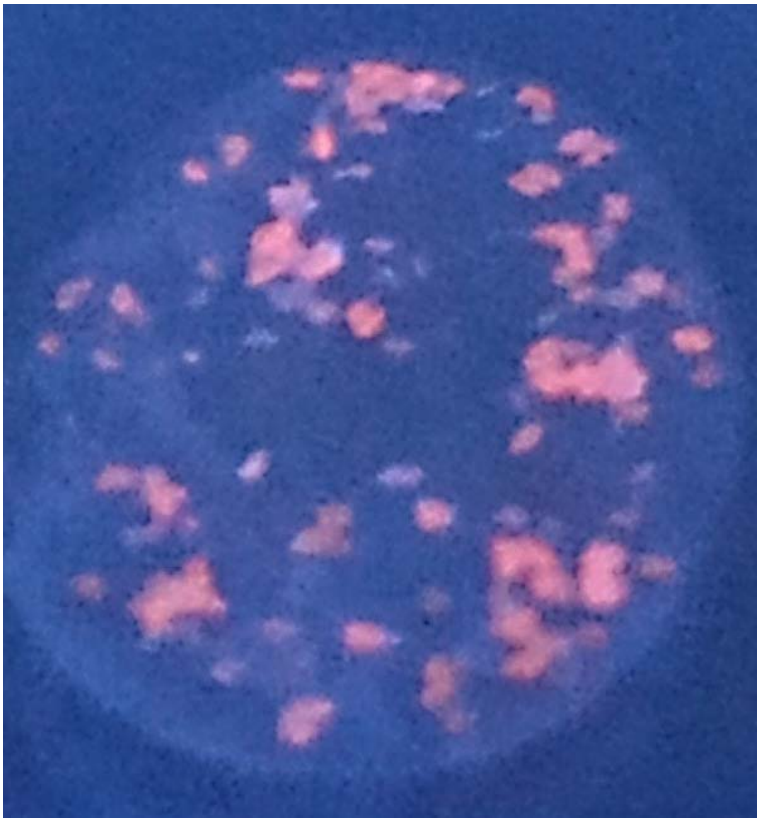

Figure S44. Photograph of the crystals of Ag_{14} under 365 nm UV-light illumination. Red luminescence was observed from the crystals.

Table S1. Crystal data, and structure refinement for Ag_{14} NC

Identification code	Arijit Ag_{14} NC	
Empirical formula	C_{228} H_{240} Ag_{14} Ag_2 B_{60} P_{12} S_{13}	
Formula weight	6143.13	
Temperature	293(2) K	
Wavelength	0.71073 Å	
Crystal system	Triclinic	
Space group	P -1	
Unit cell dimensions	a = 19.18(5) Å	a= 68.50(12)°.
	b = 19.19(4) Å	b= 82.39(19)°.
	c = 24.08(9) Å	g = 60.44(7)°.
Volume	7160(36) $Å^3$	
Z	1	
Density (calculated)	1.425 Mg/m^3	
Absorption coefficient	1.273 mm^{-1}	
F(000)	3048	
Crystal size	0.150 x 0.100 x 0.050 mm^3	
Theta range for data collection	2.926 to 18.000°.	
Index ranges	-16<=h<=16, -16<=k<=16, -20<=l<=20	
Reflections collected	67889	
Independent reflections	9814 [R(int) = 0.2609]	
Completeness to theta = 18.000°	99.5 %	
Absorption correction	Semi-empirical from equivalents	
Max. and min. transmission	0.7230 and 0.5910	
Refinement method	Full-matrix least-squares on F^2	
Data / restraints / parameters	9814 / 1854 / 1483	
Goodness-of-fit on F^2	1.613	
Final R indices [I>2sigma(I)]	R1 = 0.1869, wR2 = 0.4247	
R indices (all data)	R1 = 0.2756, wR2 = 0.4815	
Extinction coefficient	n/a	
Largest diff. peak and hole	1.783 and -2.024 $e.Å^{-3}$	

Table S2. Atomic coordinates (x 10^4) and equivalent isotropic displacement parameters ($Å^2$x 10^3) for Ag_{14}. U(eq) is defined as one third of the trace of the orthogonalized U^{ij} tensor.

	x	y	z	U(eq)
Ag(1)	5001(3)	3917(2)	5473(2)	134(2)
Ag(2)	3826(3)	5609(2)	4925(3)	134(2)
Ag(3)	4994(3)	5228(3)	5727(3)	136(2)
Ag(4)	6632(3)	5670(4)	5568(2)	141(2)
Ag(5)	3381(3)	7096(3)	3325(2)	133(2)
Ag(6)	6359(3)	2512(3)	4743(3)	143(2)
Ag(7)	3842(4)	4752(4)	6110(3)	188(2)
Ag(8)	1088(2)	4138(2)	9333(2)	81(1)
C(7)	7620(20)	6930(20)	4940(20)	95(8)
C(8)	7747(19)	6730(30)	4419(19)	99(9)
C(9)	7950(20)	7110(30)	3850(20)	110(10)
C(10)	8060(30)	7780(30)	3830(20)	116(10)
C(11)	7910(30)	8070(30)	4317(19)	111(10)
C(12)	7720(30)	7640(20)	4870(20)	102(9)
C(13)	8480(30)	5470(30)	5932(19)	100(9)
C(14)	9190(20)	5460(30)	5687(19)	90(10)
C(15)	9960(30)	4780(30)	5940(20)	108(11)
C(16)	9970(30)	4130(30)	6460(20)	110(12)
C(17)	9280(20)	4090(30)	6720(20)	111(12)
C(18)	8550(30)	4780(30)	6452(19)	101(11)
C(19)	7110(30)	6970(30)	6050(20)	131(10)
C(20)	7590(30)	6890(30)	6480(20)	138(11)
C(21)	7320(30)	7430(30)	6820(20)	144(12)
C(22)	6560(30)	8120(30)	6800(20)	159(13)
C(23)	6130(30)	8140(30)	6360(20)	160(13)
C(24)	6330(30)	7640(30)	6000(20)	150(12)
C(25)	8290(20)	1240(20)	4220(20)	100(9)
C(26)	9060(20)	540(30)	4330(20)	105(11)
C(27)	9740(30)	560(30)	4050(20)	116(12)

C(28)	9580(20)	1310(20)	3580(20)	93(10)
C(29)	8830(20)	2020(20)	3450(20)	88(10)
C(30)	8160(20)	1980(20)	3738(18)	80(9)
C(31)	7770(30)	270(30)	5290(20)	117(10)
C(32)	7810(30)	390(30)	5810(20)	118(11)
C(33)	8080(30)	-370(30)	6300(20)	136(12)
C(34)	8260(30)	-1210(30)	6420(20)	137(13)
C(35)	8240(30)	-1200(30)	5850(20)	132(12)
C(36)	8050(30)	-560(30)	5290(20)	122(11)
C(37)	6960(30)	860(30)	4080(30)	154(11)
C(38)	6290(30)	740(30)	4280(20)	164(11)
C(39)	5940(30)	500(30)	3970(20)	169(12)
C(40)	6370(30)	410(30)	3450(30)	161(12)
C(41)	7030(30)	510(30)	3250(20)	152(11)
C(42)	7360(30)	770(30)	3570(20)	147(11)
C(43)	3440(40)	8170(30)	1710(30)	135(11)
C(44)	4190(40)	7430(40)	1860(30)	166(14)
C(45)	4600(40)	7470(40)	1330(30)	174(15)
C(46)	4470(40)	8160(40)	820(30)	175(16)
C(47)	3760(40)	8910(40)	790(30)	182(16)
C(48)	3290(40)	8960(40)	1280(30)	163(14)
C(49)	2230(40)	7710(40)	2020(30)	173(11)
C(50)	2100(40)	7030(40)	2380(30)	167(12)
C(51)	1750(40)	6790(40)	2070(30)	171(12)
C(52)	1510(40)	7070(40)	1470(20)	169(12)
C(53)	1580(40)	7790(40)	1130(30)	172(12)
C(54)	2020(40)	8010(40)	1410(30)	171(12)
C(55)	1970(30)	9130(20)	2330(30)	189(13)
C(56)	1170(30)	9470(30)	2470(20)	211(15)
C(57)	620(20)	10300(40)	2430(20)	220(17)
C(58)	780(30)	11010(30)	2230(30)	221(17)
C(59)	1610(30)	10760(30)	2050(30)	209(15)
C(60)	2060(20)	9850(30)	2150(30)	195(14)
C(61)	-810(30)	4660(30)	8557(18)	97(9)
C(62)	-1090(30)	4570(30)	9130(20)	109(11)
C(63)	-1880(20)	4780(40)	9270(20)	120(12)

C(64)	-2330(30)	5000(40)	8763(19)	119(12)
C(65)	-2170(20)	5200(30)	8160(20)	114(11)
C(66)	-1340(20)	4920(30)	8090(20)	111(10)
C(67)	680(30)	3630(30)	8150(20)	103(11)
C(68)	390(40)	3100(30)	8220(30)	160(20)
C(69)	780(40)	2400(40)	8000(30)	180(30)
C(70)	1610(40)	2290(40)	7830(30)	150(20)
C(71)	2020(40)	2800(30)	7740(40)	190(40)
C(72)	1500(30)	3410(40)	7880(20)	113(17)
C(73)	30(20)	5510(30)	7785(18)	76(8)
C(74)	90(20)	5530(30)	7191(17)	84(9)
C(75)	-70(30)	6260(30)	6690(20)	91(10)
C(76)	-120(30)	6860(30)	6900(20)	95(10)
C(77)	-120(30)	6860(30)	7479(18)	92(9)
C(78)	-10(20)	6130(20)	7970(19)	83(8)
C(79)	2510(20)	4550(30)	8270(20)	94(9)
C(80)	2110(30)	5120(30)	7714(18)	109(12)
C(81)	2410(30)	4990(30)	7170(20)	110(12)
C(82)	3080(30)	4250(30)	7160(20)	118(13)
C(83)	3460(30)	3730(30)	7730(19)	126(13)
C(84)	3210(30)	3810(30)	8280(20)	121(13)
C(85)	1680(30)	5900(30)	8770(30)	126(10)
C(86)	2070(30)	6370(30)	8350(30)	133(12)
C(87)	1760(40)	7190(40)	8290(30)	134(12)
C(88)	1050(30)	7630(40)	8500(30)	138(13)
C(89)	640(30)	7180(30)	8890(30)	138(13)
C(90)	990(30)	6270(30)	9090(30)	127(12)
C(91)	2920(30)	4290(40)	9430(20)	137(11)
C(92)	3520(30)	4520(40)	9320(20)	150(12)
C(93)	4170(30)	4170(40)	9730(20)	156(13)
C(94)	4210(30)	3490(40)	10240(20)	154(13)
C(95)	3610(30)	3270(40)	10420(20)	152(13)
C(96)	2960(30)	3720(40)	10000(20)	138(12)
C(97)	2010(30)	2340(30)	10710(20)	133(9)
C(98)	1730(20)	3030(30)	10910(20)	137(10)
C(99)	1890(20)	2730(30)	11520(20)	142(10)

C(100)	2250(30)	1920(30)	11970(20)	156(11)
C(101)	2510(30)	1280(40)	11720(20)	157(10)
C(102)	2400(30)	1490(30)	11100(20)	151(10)
C(103)	1160(40)	2050(30)	10000(30)	247(16)
C(104)	1520(40)	1160(30)	10160(30)	256(17)
C(105)	1180(40)	670(40)	10170(30)	259(17)
C(106)	370(40)	1050(30)	10010(30)	257(17)
C(107)	100(40)	1910(30)	9870(30)	256(17)
C(108)	350(40)	2500(30)	9830(30)	249(17)
C(109)	2770(20)	2010(30)	9690(20)	210(14)
C(110)	3490(30)	1660(30)	10030(20)	217(16)
C(111)	4250(20)	1230(30)	9790(20)	226(17)
C(112)	4220(20)	1180(40)	9210(20)	229(18)
C(113)	3480(30)	1570(40)	8890(20)	222(17)
C(114)	2740(20)	1970(30)	9130(20)	214(16)
C(1)	1980(30)	6120(30)	4990(30)	106(5)
C(2)	2020(30)	7090(30)	4530(30)	98(5)
B(2)	1100(30)	8060(40)	4740(30)	101(6)
B(4)	1230(30)	7710(40)	4040(30)	96(6)
B(1)	1680(30)	6660(30)	4200(30)	98(5)
B(3)	1720(40)	6960(40)	5210(30)	106(5)
B(5)	1120(40)	6470(40)	5380(30)	112(6)
B(6)	1100(30)	6210(40)	4730(30)	106(6)
B(7)	580(30)	7610(40)	5320(30)	108(7)
B(8)	210(40)	7100(40)	4900(30)	108(7)
B(9)	560(30)	7270(40)	4100(30)	100(6)
B(10)	310(40)	8060(40)	4500(30)	103(7)
C(3)	4430(30)	5970(30)	6850(20)	109(6)
C(4)	5580(30)	5240(30)	6940(20)	97(6)
B(17)	5000(30)	6600(40)	7330(30)	109(6)
B(18)	5890(30)	5710(40)	7210(30)	100(6)
B(11)	4860(30)	5200(40)	8010(30)	114(7)
B(12)	4360(40)	6340(40)	7820(30)	119(7)
B(13)	5500(40)	5570(40)	7870(30)	110(7)
B(14)	5880(40)	4730(40)	7650(30)	104(7)
B(15)	4930(30)	4980(40)	7350(30)	107(6)

B(16)	4060(40)	5870(40)	7500(30)	120(7)
B(19)	5100(30)	6370(40)	6720(30)	100(6)
B(20)	4120(40)	6830(50)	7070(30)	114(7)
C(5)	5150(30)	2220(30)	6560(20)	93(5)
C(6)	5010(20)	2080(30)	5920(20)	85(5)
B(21)	5980(30)	1480(30)	6350(30)	91(5)
B(22)	5950(30)	540(40)	6810(30)	95(6)
B(23)	5630(30)	970(30)	6090(30)	89(6)
B(24)	4490(30)	1590(30)	6050(30)	87(6)
B(25)	4270(30)	2330(40)	6320(30)	90(5)
B(26)	4670(30)	1820(40)	7070(30)	96(6)
B(27)	4330(30)	1340(40)	6780(30)	93(6)
B(28)	5130(30)	740(40)	7300(30)	98(7)
B(29)	5050(30)	590(40)	6620(30)	93(6)
B(30)	5680(30)	1290(40)	7100(30)	97(6)
P(1)	7456(7)	6306(8)	5631(6)	75(4)
P(2)	7394(7)	1200(8)	4579(7)	87(4)
P(3)	2722(9)	8048(9)	2313(8)	116(5)
P(4)	2065(7)	4721(8)	8972(6)	74(3)
P(5)	218(7)	4463(8)	8445(6)	74(3)
P(6)	1738(8)	2545(9)	9942(7)	94(4)
S(1)	2813(8)	5124(8)	5234(7)	99(4)
S(2)	2897(7)	7116(7)	4375(7)	90(3)
S(3)	3890(8)	6082(8)	6220(7)	111(4)
S(4)	4987(7)	2822(8)	5195(7)	93(3)
S(5)	5123(8)	3172(9)	6579(7)	104(3)
S(6)	6096(7)	4801(9)	6413(6)	91(3)
S(7)	0	5000	10000	71(5)

REFERENCES

1. Baše, T.; Holub, J.; Fanfrlík, J.; Hnyk, D.; Lane, P. D.; Wann, D. A.; Vishnevskiy, Y. V.; Tikhonov, D.; Reuter, C. G.; Mitzel, N. W. Icosahedral Carbaboranes with Peripheral Hydrogen–Chalcogenide Groups: Structures from Gas Electron Diffraction and Chemical Shielding in Solution. *Chem. - A Eur. J.* **2019**, *25*, 2313–2321.

2. Baše, T.; Bastl, Z.; Plzák, Z.; Grygar, T.; Plešek, J.; Carr, M. J.; Malina, V.; Šubrt, J.; Boháček, J.; Večerníková, E.; Kříž, O. Carboranethiol-Modified Gold Surfaces. A Study and Comparison of Modified Cluster and Flat Surfaces. *Langmuir* **2005**, *21* (17), 7776–7785.

3. Bootharaju, M. S.; Dey, R.; Gevers, L. E.; Hedhili, M. N.; Basset, J. M.; Bakr, O. M. A New Class of Atomically Precise, Hydride-Rich Silver Nanoclusters Co-Protected by Phosphines. *J. Am. Chem. Soc.* **2016**, *138*, 13770–13773.

4. Ghosh, A.; Bodiuzzaman, M.; Nag, A.; Jash, M.; Baksi, A.; Pradeep, T. Sequential Dihydrogen Desorption from Hydride-Protected Atomically Precise Silver Clusters and the Formation of Naked Clusters in the Gas Phase. *ACS Nano* **2017**, *11*, 11145–11151.

5. Li, J. R.; Zhou, H. C. Bridging-Ligand-Substitution Strategy for the Preparation of Metal-Organic Polyhedra. *Nat. Chem.* **2010**, *2*, 893–898.

6. Mallick, A.; Garai, B.; Díaz, D. D.; Banerjee, R. Hydrolytic Conversion of a Metal-Organic Polyhedron into a Metal-Organic Framework. *Angew. Chemie - Int. Ed.* **2013**, *52*, 13755–13759.

7. Suzuki, K.; Tominaga, M.; Kawano, M.; Fujita, M. Self-Assembly of an M_6L_{12} Coordination Cube. *Chem. Commun.* **2009**, 1638–1640.

8. Enkovaara, J.; Rostgaard, C.; Mortensen, J. J.; Chen, J.; Dułak, M.; Ferrighi, L.; Gavnholt, J.; Glinsvad, C.; Haikola, V.; Hansen, H. A.; Kristoffersen, H. H.; Kuisma, M.; Larsen, A. H.; Lehtovaara, L.; Ljungberg, M.; Lopez-Acevedo, O.; Moses, P. G.; Ojanen, J.; Olsen, T.; Petzold, V *et. al*. Electronic Structure Calculations with GPAW: A Real-Space Implementation of the Projector Augmented-Wave Method. *J. Phys. Condens. Matter* **2010**, *22* (253202), 1–24.

9. Mortensen, J. J.; Hansen, L. B.; Jacobsen, K. W. Real-Space Grid Implementation of the Projector Augmented Wave Method. *Phys. Rev. B - Condens. Matter Mater. Phys.* **2005**, *71* (035109), 1–11.

10. Perdew, J. P.; Burke, K.; Ernzerhof, M. Generalized Gradient Approximation Made Simple. *Phys. Rev. Lett.* **1996**, *77* (18), 3865–3868.

11. Gavnholt, J.; Olsen, T.; Engelund, M.; Schiøtz, J. δ Self-Consistent Field Method to Obtain Potential Energy Surfaces of Excited Molecules on Surfaces. *Phys. Rev. B - Condens. Matter Mater. Phys.* **2008**, *78* (075441), 1–10.

12. Valiev, M.; Bylaska, E. J.; Govind, N.; Kowalski, K.; Straatsma, T. P.; Van Dam, H. J. J.; Wang, D.; Nieplocha, J.; Apra, E.; Windus, T. L.; De Jong, W. A. NWChem: A Comprehensive and Scalable Open-Source Solution for Large Scale Molecular Simulations.

Comput. Phys. Commun. **2010**, *181*, 1477–1489.

13. Johnson, B. G.; Fisch, M. J. An Implementation of Analytic Second Derivatives of the Gradient-Corrected Density Functional Energy. *J. Chem. Phys.* **1994**, *100*, 7429–7442.

14. Adamo, C.; Barone, V. Toward Reliable Density Functional Methods without Adjustable Parameters: The PBE0 Model. *J. Chem. Phys.* **1999**, *110*, 6158–6170.

15. Adamo, C.; Barone, V. Physically Motivated Density Functionals with Improved Performances: The Modified Perdew-Burke-Ernzerhof Model. *J. Chem. Phys.* **2002**, *116* (14), 5933–5940.

16. Jensen, F. Unifying General and Segmented Contracted Basis Sets. Segmented Polarization Consistent Basis Sets. *J. Chem. Theory Comput.* **2014**, *10* (3), 1074–1085.

17. Liang, T.; Ren, L. U. Some Studies Concerning Rotating Axes and Polyatomic Molecules. *Phys. Rev.* **1935**, *47*, 1659–1661.

18. Allouche, A. Gabedit — A Graphical User Interface for Computational Chemistry Softwares. *J. Comput. Chem.* **2011**, *32*, 174–182.